Coastal Wind-Driven Circulation in the Vicinity of a Bank. Part I: Modeling Flow over Idealized Symmetric Banks

MICHAEL M. WHITNEY

Department of Marine Sciences, University of Connecticut, Groton, Connecticut

J. S. ALLEN

College of Oceanic and Atmospheric Sciences, Oregon State University, Corvallis, Oregon

(Manuscript received 11 December 2007, in final form 7 November 2008)

ABSTRACT

This study examines how coastal banks influence wind-driven circulation along stratified continental shelves. Numerical experiments are conducted for idealized symmetric banks; the standard bank (200 km long and 50 km wide) has dimensions similar to the Heceta Bank complex along the Oregon shelf. Model runs are forced with 10 days of steady winds (0.1 Pa); upwelling and downwelling cases are compared. The bank introduces significant alongshelf variability in the currents and density fields. Upwelling-favorable winds create an upwelling front and a baroclinic jet (flowing opposite coastal-trapped wave propagation) that bend around the standard bank, approximately centered on the 90-m isobath. The upwelling jet is strongest over the upstream bank half, where it advects a tongue of dense water over the bank. There is a current reversal shoreward of the main jet at the bank center. Upwelling is most intense over the upstream part of the bank, while there is reduced upwelling and even downwelling over other bank sections. Downwelling-favorable winds create a near-bottom density front and a baroclinic jet (flowing in the direction of coastal-trapped wave propagation) that bend around the standard bank; the jet core moves from the 150-m isobath to the 100-m isobath and back over the bank. The downwelling jet is slowest and widest over the bank; there are no current reversals. Results over the bank are more similar to 2D results (that preclude alongshelf variability) than in the upwelling case. Downwelling is weakened over the bank. The density field evolution over the bank is fundamentally different from the upwelling case. Most model results for banks with different dimensions are qualitatively similar to the standard run. The exceptions are banks having a radius of curvature smaller than the inertial radius; the main jet remains detached from the coast far downstream from these banks. The lowest-order across-stream momentum balance indicates that the depth-averaged flow is geostrophic. Advection, ageostrophic pressure gradients, wind stress, and bottom stress are all important in the depth-averaged alongstream momentum balance over the bank. There is considerable variability in alongstream momentum balances over different bank sections. Across-shelf and alongshelf advection both change the density field over the bank. Barotropic potential vorticity is not conserved, but the tendency for relative vorticity changes and depth changes to partially counter each other results in differences between the upwelling and downwelling jet paths over the bank. Only certain areas of the bank have significant vertical velocities. In these areas of active upwelling and downwelling, vertical velocities at the top of the bottom boundary layer are due to either the jet crossing isobaths or bottom Ekman pumping.

1. Introduction

There is pronounced alongshelf variability in coastal upwelling and downwelling in many areas. This variability can be caused by alongshelf changes in wind forcing (e.g., Kelly 1985), by instabilities in wind-driven currents (e.g., Durski and Allen 2005), by capes and other coastline features (e.g., Arthur 1965; Johnson et al. 1980; Barth et al. 2000; Rodrigues and Lorenzzetti 2001), and by alongshelf variations in bathymetry (e.g., Peffley and O'Brien 1976; Weisberg et al. 2000; Zaytsev et al. 2003). Coastal upwelling can be intensified in the vicinity of coastal banks, such as those on the New Jersey shelf (e.g., Song et al. 2001) and the Heceta Bank complex on the Oregon continental shelf (e.g., Kosro

Corresponding author address: Michael M. Whitney, Department of Marine Sciences, University of Connecticut, 1080 Shennecossett Road, Groton, CT 06340-6097.
E-mail: michael.whitney@uconn.edu

DOI: 10.1175/2008JPO3966.1

2005; Barth et al. 2005). The baroclinic upwelling jet can move offshore and cross isobaths at these banks. Most research has focused on the upwelling regime; but it also is important to understand how alongshelf bathymetric variations influence downwelling circulation. The present process modeling study explores how coastal banks affect the wind-driven circulation along a stratified continental shelf. Upwelling and downwelling conditions are compared and contrasted to each other and to conditions along a straight shelf. This research studies the dynamic reasons underlying the wind response asymmetries such as different upwelling and downwelling intensities and different baroclinic jet paths.

Several mechanisms may influence dynamics in the vicinity of capes and banks. Inviscid theory suggests a baroclinic jet can centrifugally separate from the coast around a cape if the coastline radius of curvature is smaller than the inertial radius (V/f, the velocity magnitude divided by the planetary vorticity) of the jet (Bormans and Garrett 1989; Klinger 1994). Similarly, inviscid flow traveling along an isobath will centrifugally separate if the Rossby number involving the isobath radius of curvature ($\mathrm{Ro}_b = V/fr_b$, where r_b is the radius of curvature) exceeds one (Jiang 1995). In this situation, inertia would prevent the flow from following the isobath path, so the flow would cross isobaths. Insight from coastal hydraulics suggests that the straight shelf break and coastline curvature around capes can exert hydraulic control on the upwelling jet, leading to separation and increased upwelling downstream of the cape (Dale and Barth 2001). Other mechanisms may produce additional upwelling or downwelling around capes and banks. Arthur (1965) points to the importance of alongstream changes in relative vorticity due to jet curvature or width changes. Upwelling downstream of capes such as Punta Curaumilla, Chile, has been attributed to relative vorticity changes linked to the upwelling jet curving around the coast (e.g., Johnson et al. 1980; Figueroa and Moffat 2000). Upwelling and downwelling may be induced as coastal flows cross isobaths (Peffley and O'Brien 1976). Acceleration as a jet shoals over bathymetry can lead to increased bottom stress and sustained topographic upwelling (or downwelling) in the bottom boundary layer (e.g., Oke and Middleton 2000). Over the Heceta Bank complex, bottom stress is important (e.g., Oke et al. 2002; Gan and Allen 2005) and bottom stress curl drives upwelling along the inshore edge of the upwelling jet (e.g., Kurapov et al. 2005). It is possible that many mechanisms including local wind-driven upwelling (or downwelling), flow separation, alongstream vorticity changes, across-isobath flow, and bottom stress curl may influence the density field and wind-driven circulation in the vicinity of Heceta Bank.

A fundamental difference between the upwelling and downwelling regimes involves the evolution of the density field in response to the wind-driven across-shelf circulation and alongshelf density advection in the vicinity of a bank. There also are significant differences in the near-bottom density and flow fields for the two regimes (e.g., Trowbridge and Lentz 1991; Allen et al. 1995; Allen and Newberger 1996). Flow driven by downwelling-favorable winds can interact differently with alongshelf bathymetric variations than the flow during upwelling conditions. An asymmetric cape or bank may create qualitatively different responses for the two cases. There can be an asymmetric response even over symmetric banks. Arguments involving the conservation of potential vorticity for unforced, frictionless, barotropic flow have been put forward as a possible explanation for asymmetric response between the two wind regimes (e.g., Castelao and Barth 2006). According to this reasoning, upon shoaling over a bank each jet would develop anticyclonic vorticity, causing the upwelling jet to bend offshore and the downwelling jet to curve onshore. The importance of barotropic potential vorticity conservation during upwelling and downwelling over a bank will be examined in this study.

This study investigates the dynamics of wind-driven flow in the vicinity of coastal banks that widen and change the slope of the continental shelf. The characteristics of the upwelling and downwelling regimes are compared. Part I of this study numerically models flow over idealized banks. The standard run is a symmetric bank with similar dimensions to the Heceta Bank complex. The stratification, shelf slope, and wind forcing are representative of conditions on the Oregon continental shelf. Part II focuses on flow over the Heceta Bank complex itself (Whitney and Allen 2009). The following section of this paper describes the model configuration for Part I. Section 3 draws insight from two-dimensional model results (having no alongshelf variability). Section 4 describes the density and current fields that develop over the standard idealized bank during upwelling and downwelling conditions. Section 5 discusses flow characteristics for different latitudes and over banks with different dimensions. Upwelling and downwelling dynamics are described in section 6; the momentum and density balances are calculated and vertical velocity contributions are analyzed. The final section includes a summary and conclusions.

2. Model configuration

The Regional Ocean Modeling System (ROMS, version 2.1) is used in this study. The governing equations and differencing schemes are discussed in Haidvogel

et al. (2000) and in Shchepetkin and McWilliams (2005). ROMS is a finite-difference model that solves the hydrostatic nonlinear primitive equations. Vertical differencing is achieved with terrain-following s coordinates (Song and Haidvogel 1994). In this study, the model is run with a third-order upwind advection scheme for momentum (Shchepetkin and McWilliams 1998) and a fourth-order centered advection scheme for tracers. The horizontal pressure gradient is treated with a spline density Jacobian (Shchepetkin and McWilliams 2003) after subtracting the background stratification. Mixing along s-coordinate surfaces is Laplacian; the horizontal viscosity and diffusivity are set at 2 $m^2\ s^{-1}$. Vertical mixing follows the Mellor–Yamada level 2.5 closure scheme (Mellor and Yamada 1982); the background vertical viscosity and diffusivity are 10^{-5} $m^2\ s^{-1}$ and 10^{-6} $m^2\ s^{-1}$, respectively. Bottom stress is calculated with a quadratic drag law using a bottom roughness of 10^{-2} m. Potential density is used in these simulations in place of individually evolving temperature and salinity.

The model domain (Fig. 1) is 200 km wide and 600 km long. A straight coast borders the east side of the domain. The x and y axes are positive in the eastward and northward directions, respectively. The origin is at the coast in the center of the domain. Horizontal resolution is 2 km throughout the domain. Vertical resolution is supplied by 40 s-coordinate levels. The nonlinear stretching of these s coordinates is set using the equations in Song and Haidvogel (1994) with $h_c = 10$ m, $\theta = 5$, and $b = 1$. This s-coordinate configuration allows for better resolution near the surface and bottom. The domain is periodic in the y direction. Free-slip conditions are applied along the coast. On the offshore boundary, gravity wave radiation is applied to surface elevation and depth-averaged tangential velocity $\overline{v}$. A Flather condition links the depth-averaged boundary-normal velocity $\overline{u}$ to the surface elevation. Flow through the offshore open boundary is constrained to have zero net volume flux. Zero gradient conditions are applied to the vertically varying velocities and potential density along the offshore boundary. The model is run with time steps of 7.3 s for the depth-averaged mode and 240 s for the depth-varying mode.

The model bathymetry along the straight shelf has a slope α of 10^{-2}; this is typical of the continental shelf along the U.S. West Coast. A 10-m minimum depth is imposed next to the coast (instead of tapering to zero at the shore) and a 1000-m maximum depth is imposed beyond 100 km offshore. The average slope is the same in the vicinity of the bank since the coast and the 1000-m isobath are straight. The slope is gentler inshore of the bank edge and steeper offshore. The 200-m isobath defines the bank edge in these model runs. The bank is formed by bending this isobath offshore with a raised cosine function of wavelength L and width W (Fig. 1). Depths increase piecewise linearly from the coast to the bank edge and offshore to the shelf edge. The minimum radius of curvature along the 200-m isobath is at the bank crest ($y = 0$ km): $r_b = L^2/2\pi^2 W$. The standard model run has a bank with $L = 200$ km and $W = 50$ km ($r_b = 40.5$ km). This bank geometry is the same scale as the bathymetry of the Heceta Bank complex (on the Oregon shelf) studied in Part II. The planetary vorticity f is 1.022×10^{-4} s^{-1} (the value at 44.5° latitude); f is positive for the upwelling case and negative for the downwelling case. Varying the sign of f is equivalent to varying the wind stress sign for these symmetric bank

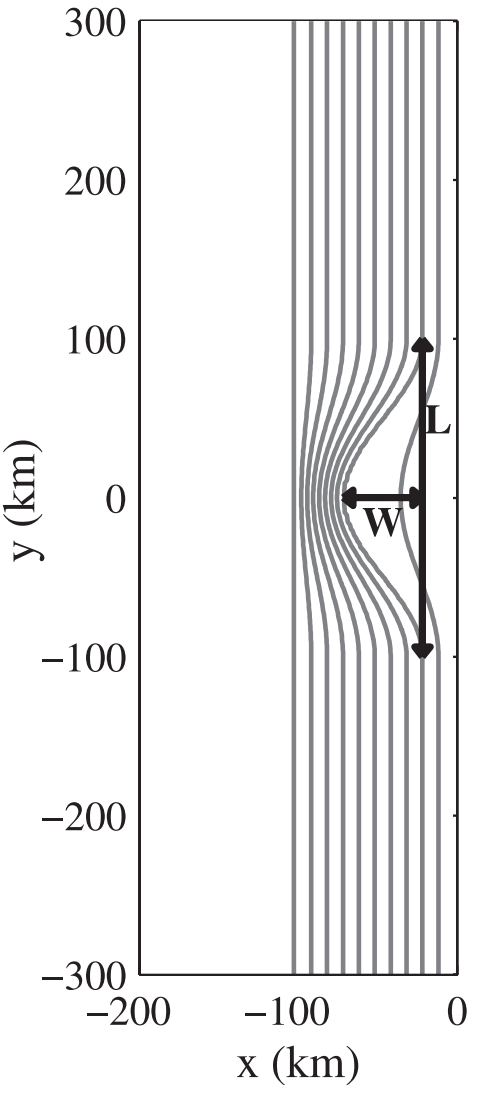

FIG. 1. Model domain and bathymetry for the standard run ($L = 200$ km, $W = 50$ km); isobaths are contoured with a 100-m interval. The slope along the straight shelf is 10^{-2}. The symmetric bank is constructed by bending the 200-m isobath with a raised cosine function of wavelength L and width W.

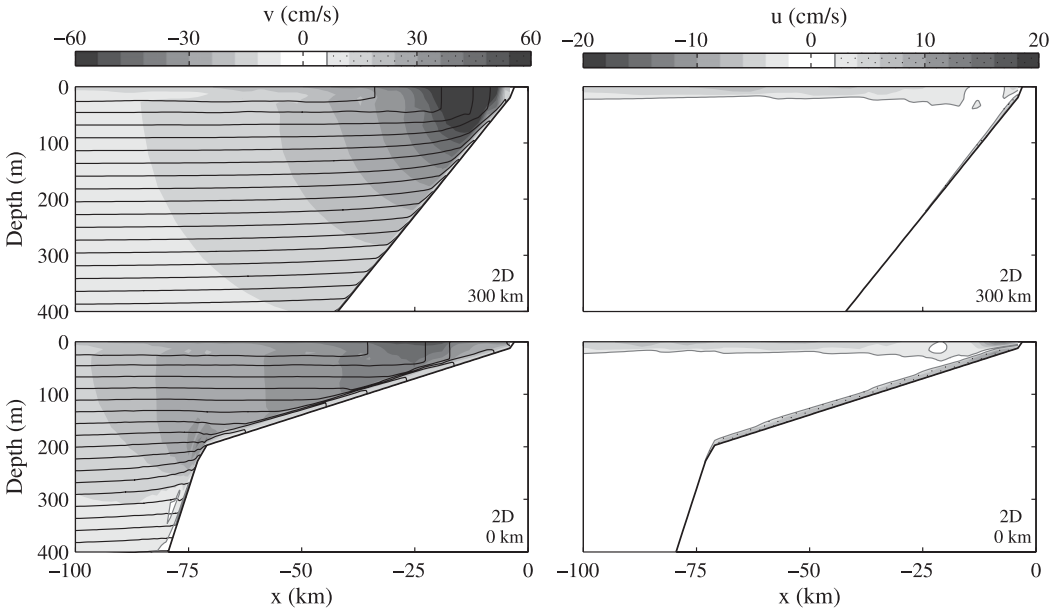

FIG. 2. Cross sections of 2D upwelling solutions on day 10. (top) The shelf results ($y = 300$ km). (bottom) The bank results ($y = 0$ km). Alongshelf velocity (positive northward) and across-shelf velocity (positive onshore) are contoured. Isopycnals are line contoured (0.25 kg m^{-3} interval) on the alongshelf velocity graphs.

runs. Choosing to vary the sign of f facilitates intercomparison between the upwelling and downwelling cases since alongshelf flow is in the same direction for both cases. The model is initialized with zero velocities and constant stratification. The initial buoyancy frequency N is 10^{-2} s^{-1}. The slope Burger number $N^2\alpha^2/f^2$ on the shelf is one and the internal Rossby radius Nh/f is 20 km for $h = 200$ m and 5 km for $h = 50$ m. The model is forced with a spatially uniform alongshelf wind stress τ^{sy} of -0.1 Pa (blowing toward the south). After a half-day ramping period, the wind stress remains constant for the 10-day duration of the run. All results discussed in this paper have been averaged over an inertial period (17 h). Other model runs (described in section 5) vary the length and width of the bank. The initial stratification and wind stress are held constant among the runs to focus on the effects of altering bank geometry.

3. Two-dimensional solutions

There should be pronounced alongshelf variability in the vicinity of banks. Therefore, the wind-driven flow regime should exhibit three-dimensional (3D) dynamics. Two-dimensional (2D) solutions (variable across shelf and with depth, but assumed uniform alongshelf) using local straight shelf and bank topography, nevertheless, are useful benchmarks. Differences between the 2D solutions over different topography may imply some of the features of the 3D flow field. The 2D model results are run with the same settings described in section 2. The bathymetry is from a shelf cross section ($y = 300$ km) and a bank section ($y = 0$ km). Figures 2 and 3, respectively, show cross sections of the 2D upwelling ($\tau^{sy} < 0, f > 0$) and downwelling ($\tau^{sy} < 0, f < 0$) solutions after 10 days of steady winds.

The density field during upwelling conditions (Fig. 2) exhibits upwelled isopycnals and a nearshore density front. The upwelling is driven by offshore surface Ekman transport and compensating onshore flow in the interior and bottom boundary layer. A baroclinic coastal jet flowing alongshelf in the direction of the winds (opposite the direction of coastal-trapped wave propagation) is in geostrophic balance with the across-shelf pressure gradient; the jet is in thermal wind balance with the upwelled isopycnals. Vertical velocities (not shown) are associated with upslope flow concentrated in the bottom layer and fluctuating circulation cells at the surface near the upwelling front. These results are consistent with previous 2D upwelling studies (Allen et al. 1995). Over the straight shelf, the jet core is centered over the 90-m isobath (9 km offshore) with an 80 cm s^{-1} maximum surface velocity. Over the gentle slope of the bank bathymetry (lower panels), the baroclinic jet is wider and slower (with less horizontal shear) than over the shelf bathymetry. The velocity core and upwelling front are located farther offshore over the bank. The near-surface upwelling zone has the same vertical extent and degree of density change.

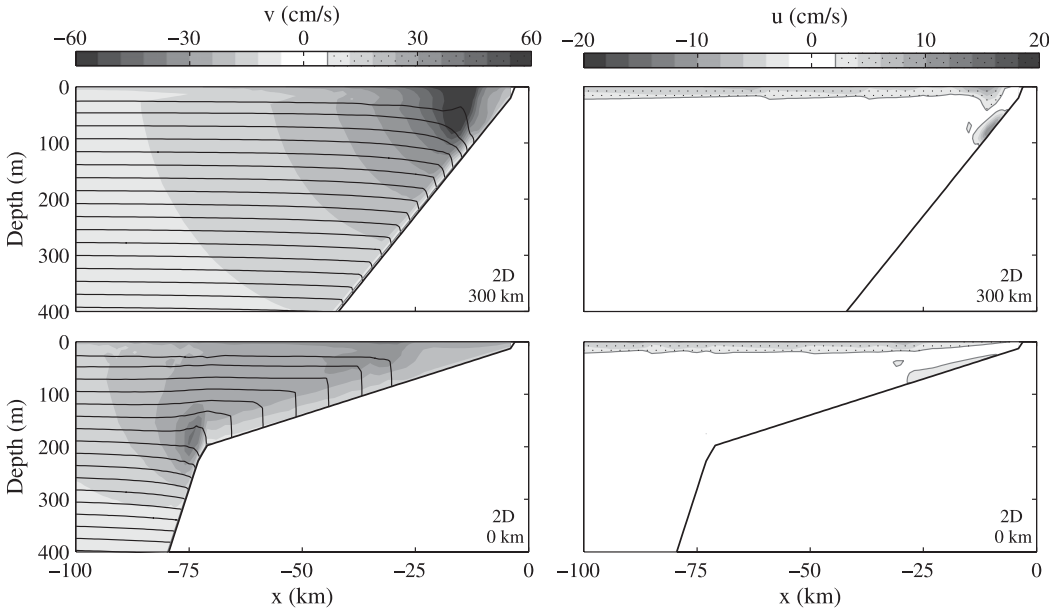

FIG. 3. Cross sections of 2D downwelling solutions on day 10. Panels are arranged as in Fig. 2.

The density field during downwelling conditions (Fig. 3) exhibits downwelled isopycnals and a near-bottom density front close to the coast. The downwelling is driven by onshore surface Ekman transport and offshore return flow below the surface layer. As in the upwelling cases, a baroclinic alongshelf jet develops in geostrophic balance with the across-shelf pressure gradient; the jet is in thermal wind balance with the sloped isopycnals. It flows in the same direction as the winds (in the direction of coastal-trapped wave propagation). The downwelling jet and upwelling jet flow in the same direction in these experiments because the sign of f is switched instead of the wind stress sign. Vertical velocities (not shown) are associated with the downwelling front and symmetric instabilities in the bottom mixed layer. The stratified 2D downwelling regime and symmetric instabilities have been described previously by Allen and Newberger (1996). The upwelling and downwelling cases have similar lateral and vertical scales for the baroclinic jet. The downwelling jet core, however, is farther offshore and slower: over the straight shelf the core is centered over the 150-m isobath (15 km offshore) with a 50 cm s^{-1} maximum velocity. The downwelling jet has less vertical shear, which is linked through thermal wind balance to the smaller across-shelf density gradient. There is no surface density change during downwelling (and no near-surface across-shelf density gradient); the density change signature is concentrated near the bottom. The downwelling circulation creates a thick bottom mixed layer, whereas in upwelling the region near the bottom boundary is highly stratified (Trowbridge and Lentz 1991). As in the upwelling case, the downwelling jet is wider, slower, and farther offshore over the bank than over the straight shelf.

The differences in the geostrophic jet over the shelf and bank result in differences in the across-shelf pressure gradient. Figure 4 shows the across-shelf sea level variations over the shelf and bank bathymetry for the 2D upwelling and downwelling cases. In both cases, the surface elevation displacement is larger over the bank at every distance offshore. These differences suggest the existence of alongshelf pressure gradients over the bank in the 3D case. The 2D upwelling results predict a sea level depression over the bank that might balance a geostrophic flow offshore around the upstream side and back onshore around the downstream half. The 2D downwelling results imply a sea level dome that also might balance a geostrophic jet flowing around the bank. These alongshelf variations in local 2D upwelling and downwelling dynamics may influence the 3D flow field. There are strong similarities between the 2D and 3D sea level trends (included in Fig. 4) over the shelf and bank. Alongshelf advection of momentum and density, however, lead to significant departures from 2D dynamics in the vicinity of the bank.

4. Results for the standard run

The standard run involves 3D solutions over a cosine bank with dimensions (L = 200 km, W = 50 km) similar to the Heceta Bank complex. This section describes the velocity and density fields driven by steady wind forcing

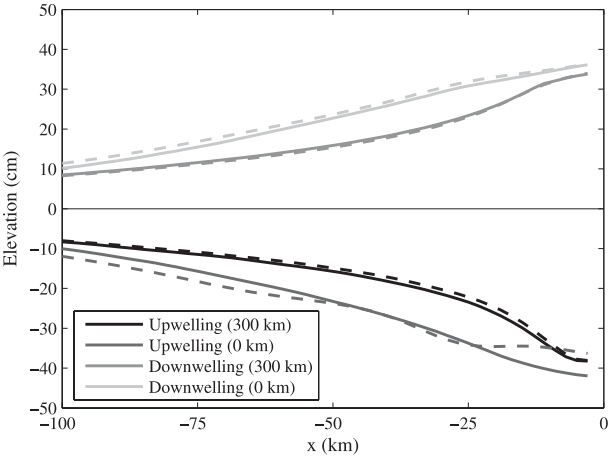

FIG. 4. Across-shelf surface elevation trends (day 10). Solid lines indicate 2D solutions and dashed lines are from 3D results. Surface elevations are negative during upwelling and positive during downwelling. The differences between shelf and bank results imply a sea level depression over the bank during upwelling and a sea level rise during downwelling.

($\tau^{sy} = -0.1$ Pa). The sign of f is changed between the upwelling ($f > 0$) and downwelling ($f < 0$) cases. The analysis in this section focuses on the flow regime after 10 days of winds.

a. Upwelling case

During the onset of upwelling-favorable winds, upwelling begins along the entire coast. At this early stage, alongshelf velocities are weak and the jet is widest over the bank. Analysis of results indicates that an alongshelf sea surface gradient develops (with sea level lowest over the bank). This pressure gradient is associated with the deflection of the geostrophic jet offshore over the upstream half of the bank and back onshore over the downstream half. As winds continue, the flow accelerates and bends around the bank with increasing curvature. Away from the bank, the upwelling front is near the coast and the circulation matches the 2D solution. By day 10 (Fig. 5a) on the straight shelf, the baroclinic jet is 40 km wide, the jet core is over the 90-m isobath, and the core velocity is 80 cm s^{-1}. The jet deflects from the coast at the bank and reattaches downstream of the bank; the jet core approximately follows the 90-m isobath. Streamlines offshore of the main jet are shallower over the bank than along the straight shelf. The jet is fastest over the upstream part of the bank and slowest over the downstream half. On the bank inshore of the main jet, flow reverses then turns anticyclonically and flows downstream again along the coast.

Depth-averaged density contours initially are parallel to isobaths, but upwelling and advection modify the density field. By day 10 (Fig. 5a), a tongue of high-density water extends over the upstream half of the bank along the inshore edge of the jet. The evolution of this feature suggests that the dense waters have been advected from the upstream bank edge, where coastal density is highest. Figure 6a indicates that bottom density increases due to upwelling are concentrated inshore of the 200-m isobath. The upstream edge of the bank is the area with the largest density change. Density increases are more pronounced on the upstream half of the bank than on the downstream half, where density changes are smaller than on the straight shelf. There are two areas of bottom density increase over the bank: inshore of the main jet over the upstream half and downstream between the 100- and 200-m isobaths where the jet converges as it flows back toward the coast.

The relative vorticity of the depth-averaged flow gives information about the horizontal shear, the importance of advective terms, and the flow curvature. Relative vorticity ζ can be expressed in natural coordinates as

$$\zeta = -\frac{\partial V}{\partial n} + \frac{V}{r}. \tag{1}$$

In this coordinate system, s is aligned with transport streamlines (positive in the flow direction) and n is across stream (positive to the left looking downstream). The vorticity associated with lateral shear of the jet is given by the first term in (1), which represents the across-stream derivative of depth-averaged velocity V. The second term in (1) is the vorticity associated with alongstream changes in streamline orientation ($\partial\theta/\partial s$). This curvature vorticity is the speed divided by the radius of curvature of the flow (where $1/r = \partial\theta/\partial s$). The ratio of the curvature vorticity V/r and planetary vorticity f is a Rossby number $\mathrm{Ro} = V/fr$. This Rossby number measures the relative importance of advection in the depth-averaged across-stream momentum equation; $r = V/f$ and $\mathrm{Ro} = 1$ for inertial motion (Holton 1992). Since this Ro definition involves the radius of curvature rather than the more common choice of either the length or width scale of the flow, the interpretation of Ro is different from usual; for instance, $\mathrm{Ro} = 0$ for any flow that follows a straight path.

The jet vorticity of the depth-averaged flow (scaled by f) is contoured for the upwelling case in Fig. 7a. The shoreward side of the jet is characterized by positive relative vorticity of order f. The seaward shear zone is wider with smaller values of negative jet vorticity (this asymmetry also is present in the surface vorticity field). Magnitudes of the jet vorticity are smaller over the downstream half of the bank, where the jet is slower and wider. The curvature vorticity scaled by f (Fig. 8a) is of order 0.1. These low Rossby number values indicate that the lowest-order across-stream momentum balance does

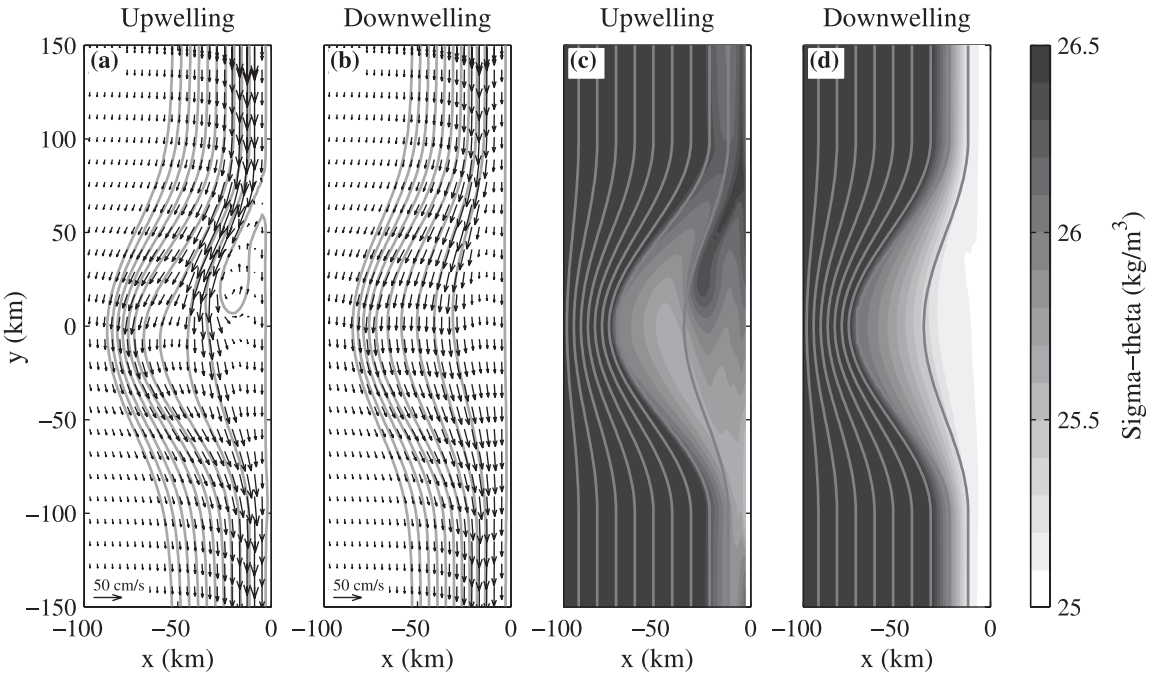

FIG. 5. Depth-averaged velocity vectors and transport streamlines (gray lines) for the standard run on day 10 during (a) upwelling and (b) downwelling. Depth-averaged density fields with isobaths contoured at a 100-m interval (gray lines) for day 10 during (c) upwelling and (d) downwelling.

not include advection even in turning regions. Curvature vorticity is largest within the jet over the upstream half of the bank. These positive values reflect the counterclockwise curving of the jet around the bank and the reversing of the flow inshore of the main jet. The positive and negative patches at the upstream bank edge, offshore bank center, and downstream bank edge are the signature of the flow bending around the bank. The Rossby number range associated with these patches is ± 0.05. The Rossby number magnitude that would be necessary for a 30 cm s^{-1} flow to follow the 200-m isobath exactly (with minimum $r_b = 40.5$ km) is $V/fr_b = \pm 0.07$. The small curvature vorticity indicates that centrifugal acceleration remains small relative to the geostrophic terms in the depth-averaged across-stream momentum balance. Depth-averaged flow does not follow isobaths exactly as it traverses the bank, even though the isobath radius of curvature is much larger than the inertial radius of the flow ($V/f < 10$ km, Ro $\ll 1$).

The cross sections at $y = 300$ km and $y = 0$ km (Fig. 9) can be compared to the 2D solutions (Fig. 2). The upwelling circulation far from the bank matches the 2D solution. There are pronounced differences over the bank ($y = 0$ km). There is a region of downwelled isopycnals at middepth on the seaward side of the main jet. The upwelling front is farther offshore and the distribution of density increases differs greatly from the 2D solution. Unlike the wide jet occupying the entire bank in the 2D run, the main jet is narrow and detached from the coast. The across-shelf circulation over the bank departs from the 2D regime of offshore transport near the surface and onshore flow concentrated in the bottom boundary layer. Vertical velocities (not shown) are upward in the nearshore upwelling region and downward in the offshore downwelling area. In some areas over the bank bottom transport is offshore. There is a secondary zone of upwelling and associated alongshelf velocities offshore of the shelf break. Secondary upwelling at a shelf break has been described previously (O'Brien and Hurlburt 1972; Hill and Johnson 1974). The discussion in this paper focuses on the main jet and the coastal upwelling front.

b. Downwelling case

Downwelling initially begins near the coast everywhere along the shelf. An alongshelf sea surface gradient develops (with sea level highest over the bank) that is consistent with the geostrophic jet curving around the bank. By day 10 (Fig. 5b), the jet is 50 km wide with its core centered over the 150-m isobath with a 50 cm s^{-1} maximum velocity on the straight shelf. Streamlines bend around the bank but do not follow isobaths exactly. The jet flows over shallower depths over the bank; the jet core shoals to the 105-m isobath at the bank

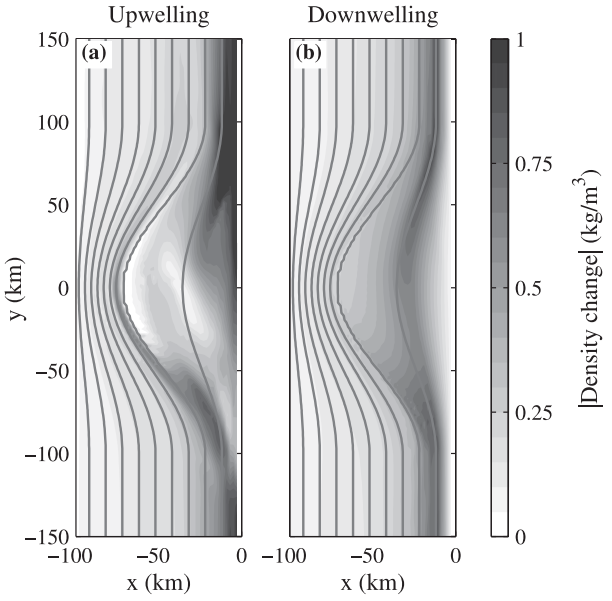

FIG. 6. Bottom density change (day 10) from the initial state during (a) upwelling and (b) downwelling. Density increases in the upwelling case and decreases in the downwelling case. Isobaths are shown as in Fig. 5.

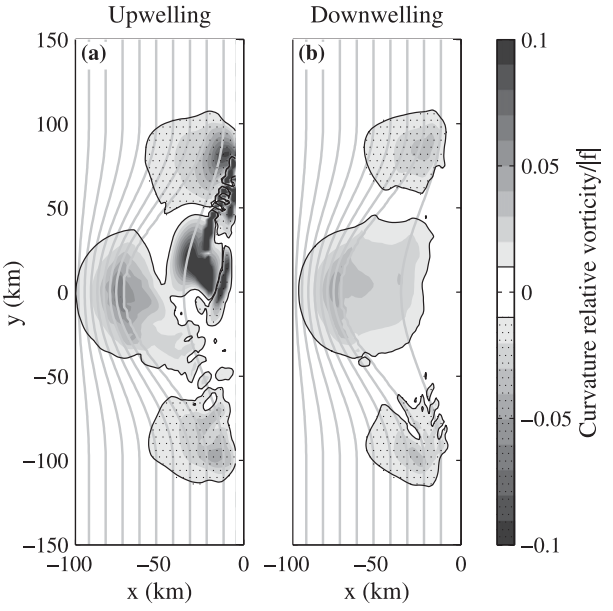

FIG. 8. Curvature relative vorticity of the depth-averaged flow (V/r) scaled by $|f|$ during (a) upwelling and (b) downwelling on day 10. Isobaths are shown as in Fig. 5. The contour range is 10 times smaller than for Fig. 7.

center. The downwelling jet is farther offshore than the upwelling jet over the straight shelf, but shoals to near the isobath that the upwelling jet occupies over the bank. Depth-averaged velocities are slowest over the bank, where the jet is widest. Unlike the upwelling flow field, jet speeds are largely symmetric about the bank center and there are no reversed currents.

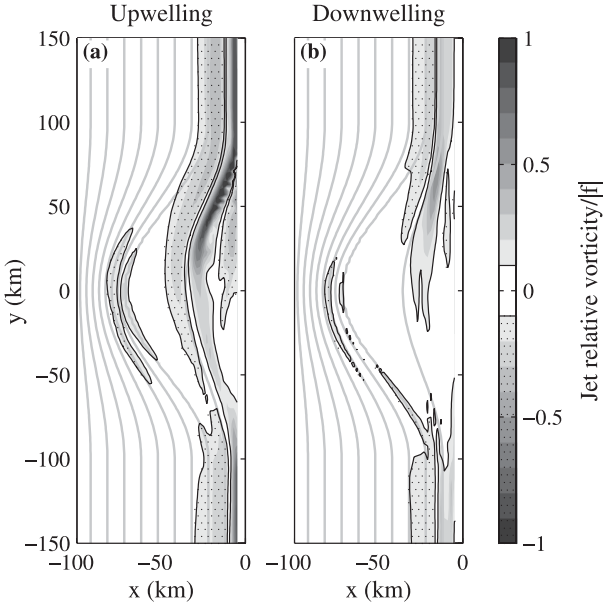

FIG. 7. Jet relative vorticity of the depth-averaged flow ($-\partial V/\partial n$) scaled by $|f|$ during (a) upwelling and (b) downwelling on day 10. Isobaths are shown as in Fig. 5.

Downwelling has decreased depth-averaged potential densities (Fig. 5b) within the 200-m isobath. The depth-averaged density contours are approximately aligned with isobaths. Density monotonically decreases toward the coast over the straight shelf and the bank. In contrast, the upwelling case (Fig. 5a) has a tongue of dense water that changes the sign of the across-shelf density gradient. In the downwelling case, bottom densities have decreased over the shelf and bank (Fig. 6b). The density changes are concentrated along the 100-m isobath. Unlike the upwelling case, there is little density change near the coast. This difference arises because the downwelling source waters are the constant-density surface waters, whereas upwelling brings increasingly dense waters from lower depths to the coast. With constant-density surface waters, the maximum possible bottom density decrease $\Delta\rho_{\mathrm{bot}}$ due to 2D downwelling is proportional to depth h; for a constant initial stratification (N^2) the maximum change is $|\Delta\rho_{\mathrm{bot}}| \leq \rho_o N^2 h/g$. With constant initial stratification, there is no similar limit on bottom density change for upwelling. The alongshelf differences in bottom density change during downwelling are less pronounced than during upwelling. Bottom density decreases most over the straight shelf; the bank is a region of reduced downwelling. Density changes are smallest over the downstream half of the bank. A region of low bottom density extends

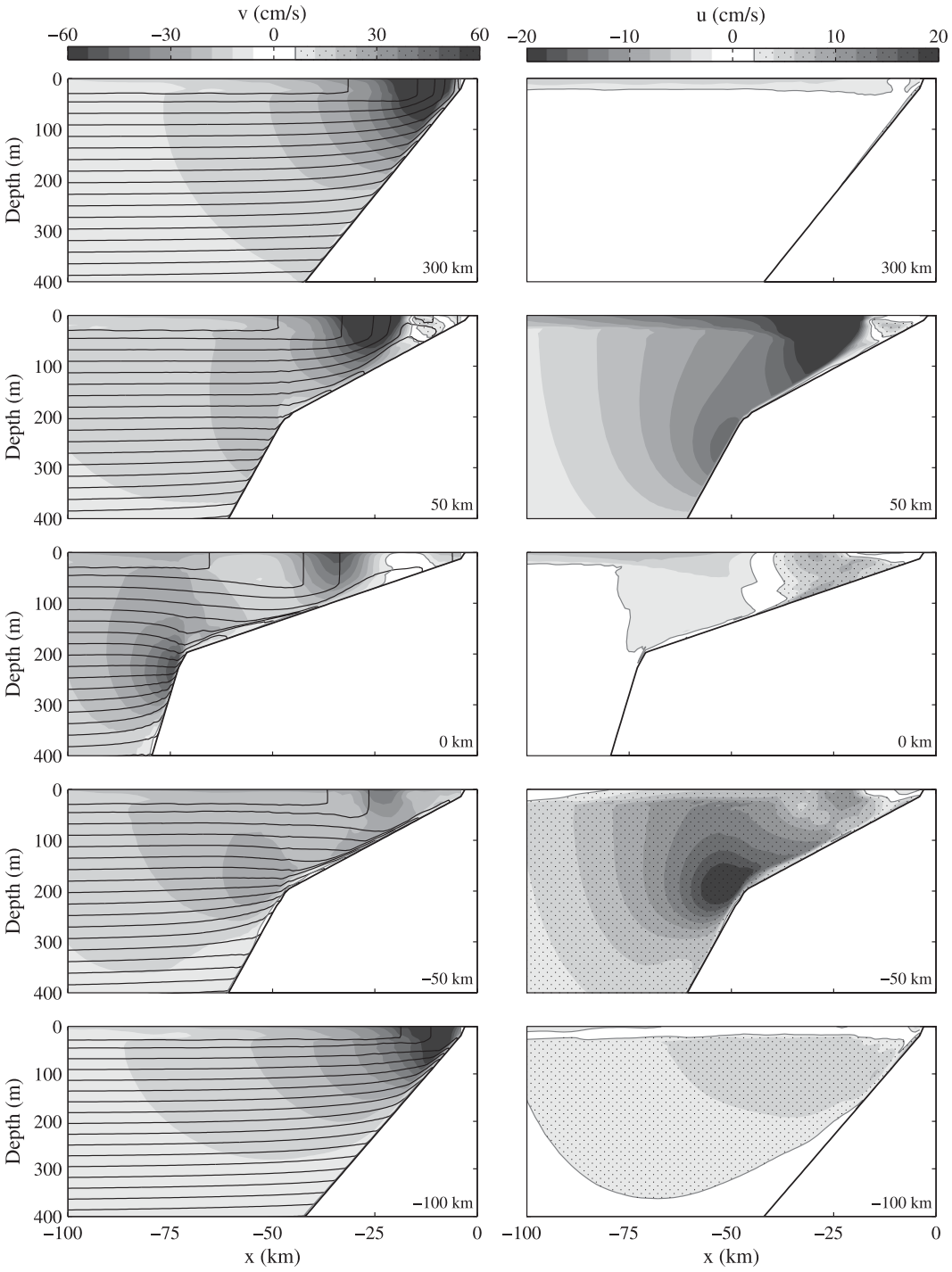

FIG. 9. Cross sections during upwelling (day 10). (top row) Results on the straight shelf (y = 300 km). (bottom rows) The sequence southward over the standard bank at a 50-km interval. Alongshelf velocity (positive northward) and across-shelf velocity (positive onshore) are color contoured. Isopycnals are line contoured (0.25 kg m^{-3} interval) on the alongshelf velocity graphs.

across the upstream half along the downwelling front. There also is a wider area of downwelled water offshore at the downstream edge of the bank.

The relative vorticity of the jet divided by $|f|$ ($f < 0$ for this case) is shown in Fig. 7b. The jet vorticity is anticyclonic ($-0.5f$) on the shoreward side of the downwelling jet. The seaward cyclonic shear zone is less intense and wider. Jet vorticity values are low over most of the bank where the jet is slowest and widest. The curvature vorticity (Fig. 8b) shows the bending of the flow around the bank. Flow turns cyclonically offshore at the upstream edge of the bank, curves anticyclonically around the bank, and turns cyclonically at the downstream edge to flow parallel to the coast again. The radius of curvature of the 200-m isobath is much larger than the inertial radius ($\mathrm{Ro}_b = V/fr_b \ll 1$). The flow curvature vorticity ($\pm 0.04f$) is less than is necessary to follow isobaths perfectly. In contrast to the upwelling case, the curvature within the core of the jet is similar to offshore.

The vertical structure of the downwelling regime is shown in the density and velocity sections (Fig. 10). The section over the straight shelf ($y = 300$ km) matches the 2D downwelling solution (Fig. 3). The baroclinic jet has the same width and depth scale as the upwelling case, but the core velocity is slower and the vertical shear is lower because of the smaller across-shelf density gradients (especially near the surface). As in the 2D solution, flow is onshore at the surface and offshore near the bottom inshore of the front. The 3D results at the bank center ($y = 0$ km) are similar to the 2D bank solution (Fig. 3). The general similarity between the 3D and 2D solutions over the bank is not seen in the upwelling case.

For all sections (Fig. 10), density decreases are concentrated in the bottom mixed layer (where isopycnals are near vertical) out to the 200-m isobath. There is weak upwarping of isopycnals at middepth over the offshore edge of the bank ($y = -25$ km to $y = 25$ km). This upwelling is not as strong as the downwelling that occurs in the upwelling case on the seaward side of the jet (Fig. 9). The alongshelf velocity sections show the detachment and reattachment to the coast as the jet travels around the bank. The interior across-shelf velocities are offshore over the upstream side of the bank and onshore over the downstream side. The influence of onshore surface Ekman transport is evident in all sections. Downstream of the bank, the density and velocity fields match the 2D shelf solution.

5. Results for other latitudes and bank dimensions

This section investigates upwelling and downwelling dynamics at different latitudes and over banks with different dimensions. It is important to identify robust flow features among the runs and differences resulting from parameter changes. Section 5a examines runs with different planetary vorticities and looks at alongstream changes in barotropic potential vorticity. Section 5b compares runs with banks of different lengths and widths. Some of these runs exhibit a higher degree of flow separation from isobaths than the standard runs.

a. Varying planetary vorticity

Upwelling and downwelling cases have been run for low-latitude ($\pm 31.5°$, $f = \pm 0.762 \times 10^{-4}$ s^{-1}), midlatitude ($\pm 44.5°$, $f = \pm 1.022 \times 10^{-4}$ s^{-1}), and high-latitude ($\pm 70°$, $f = \pm 1.371 \times 10^{-4}$ s^{-1}) conditions over the standard bank geometry; the planetary vorticity is successively increased by a factor of 1.34 from the low- to high-latitude runs. The velocity and density fields for each latitude are qualitatively similar for the standard bank. The following analysis of the jet path indicates differences among the runs. The differences between the upwelling and downwelling regimes are much stronger than the variations created by changing planetary vorticity from low- to high-latitude values.

Changing latitude modifies the potential vorticity field. The barotropic potential vorticity PV, involving the relative vorticity of the depth-averaged flow $\overline{\zeta} = \overline{v}_x - \overline{u}_y$, is defined as

$$\mathrm{PV} = \frac{\overline{\zeta} + f}{h}. \tag{2}$$

The total derivative of PV can be separated into a term involving depth changes and one involving absolute vorticity changes (relative vorticity changes on an f plane):

$$\frac{\overline{D}(\mathrm{PV})}{Dt} = -\frac{\mathrm{PV}}{h}\frac{\overline{D}h}{Dt} + \frac{1}{h}\frac{\overline{D}(\overline{\zeta} + f)}{Dt} \tag{3a}$$

with the operator

$$\frac{\overline{D}(\,)}{Dt} = \frac{\partial(\,)}{\partial t} + \overline{u}\frac{\partial(\,)}{\partial x} + \overline{v}\frac{\partial(\,)}{\partial y}. \tag{3b}$$

If barotropic potential vorticity is conserved, the two terms on the right side of (3a) offset each other and the total PV derivative is zero. Castelao and Barth (2006) suggested that barotropic potential vorticity conservation may explain some differences between upwelling and downwelling jets as they flow over banks. A shoaling flow attempting to conserve potential vorticity would generate more anticyclonic vorticity (opposite the sign of f) to conserve potential vorticity, while a flow moving over deeper waters would generate more

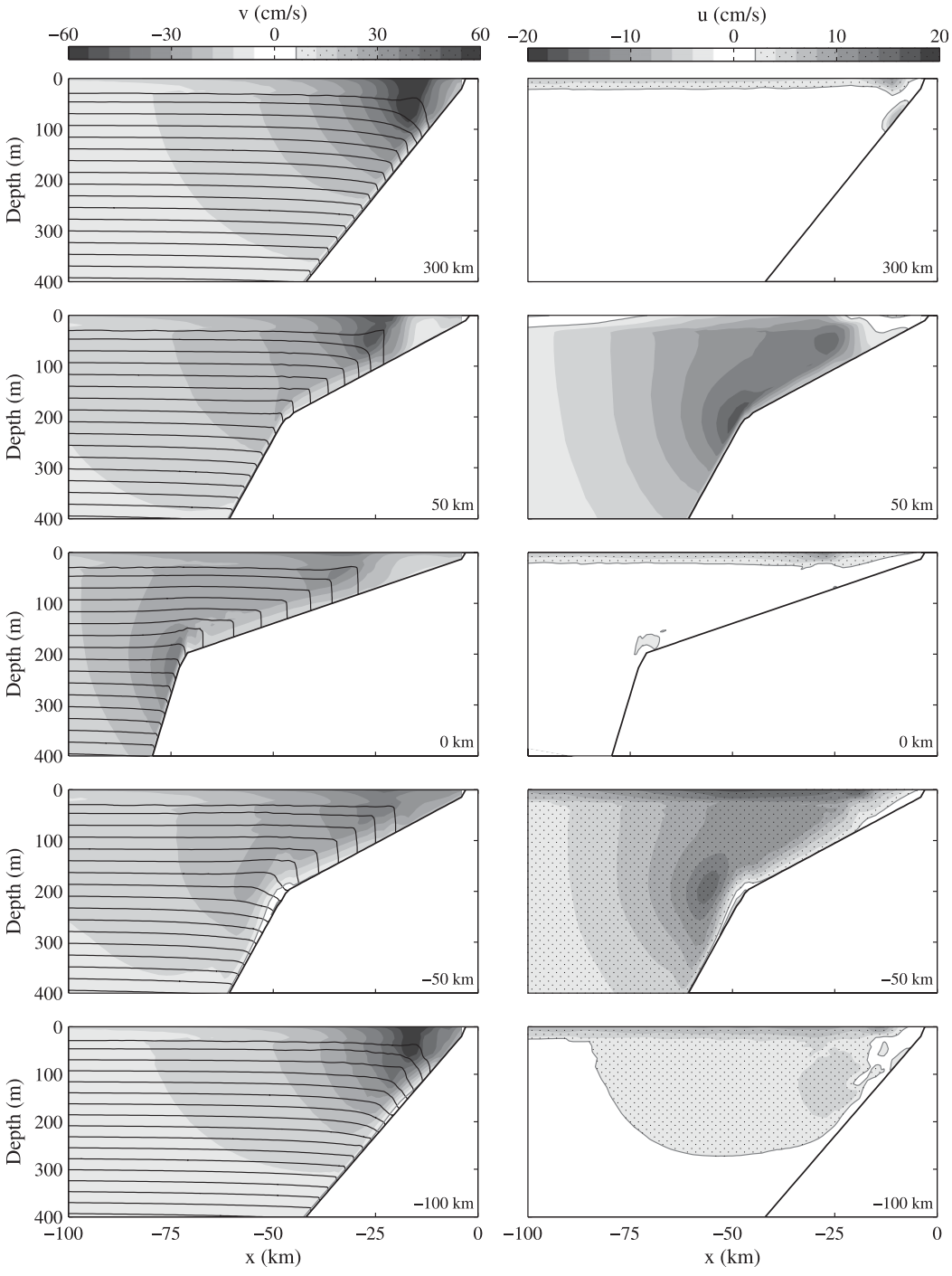

FIG. 10. Cross sections during downwelling (day 10). The panels are arranged as in Fig. 9.

cyclonic vorticity (same sign as f). After crossing isobaths (either onshore or offshore), an upwelling jet would curve back toward its initial isobath, while a downwelling jet would curve away from the original isobath. Friction and other effects, however, can become important over banks, so barotropic potential vorticity may not be conserved over banks because of frictional and baroclinic torques.

The path of the upwelling jet for low-, mid-, and high-latitude runs (Fig. 11a) is tracked by following the transport streamline that originates in the jet core over the straight shelf. In each run, the jet core originates

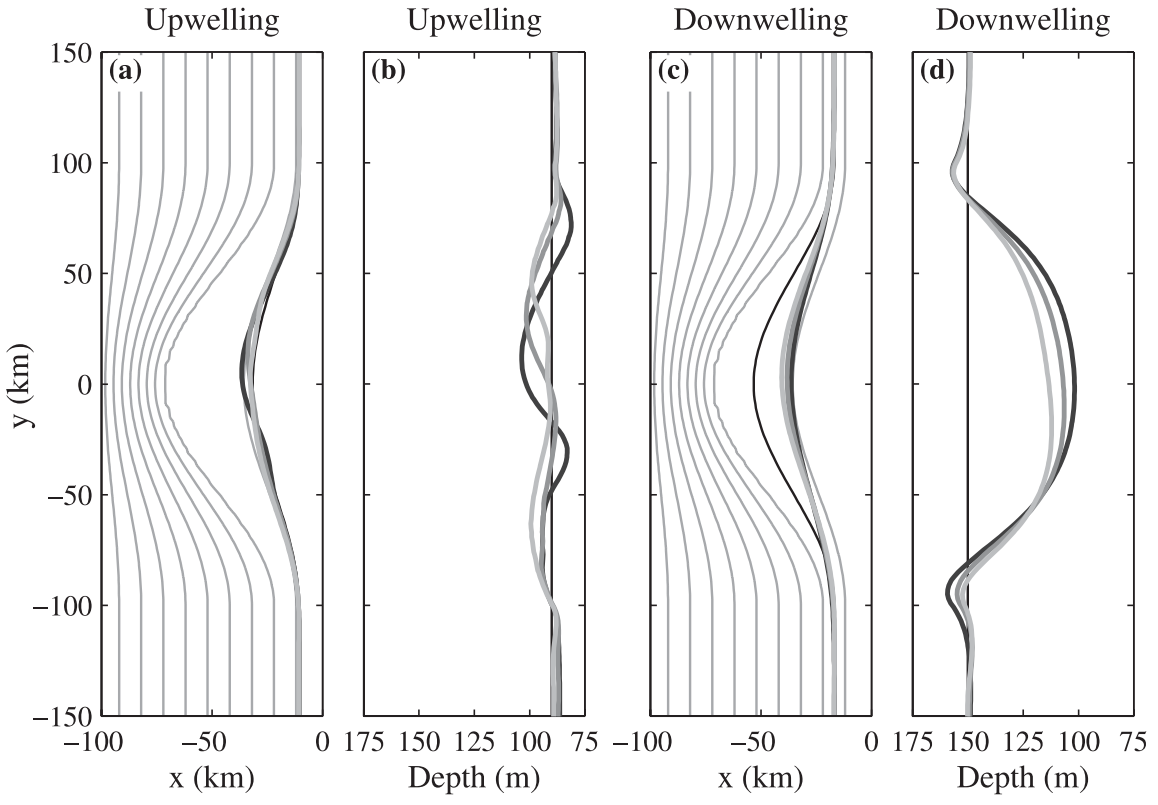

FIG. 11. Path of the streamline following the jet core for upwelling and downwelling runs with different f (day 10): (a) path during upwelling, (b) bottom depth along path during upwelling, (c) path during downwelling, (d) bottom depth along path during downwelling. The thick black, dark gray, and light gray lines are the low f (0.762×10^{-4} s^{-1}), standard f (1.022×10^{-4} s^{-1}), and high f (1.371×10^{-4} s^{-1}) results, respectively. The thin black line follows the isobath that the jet core is centered on along the straight shelf. Thin gray lines contour bathymetry at a 100-m interval.

on the 90-m isobath and oscillates around this isobath over the bank. Depths along the jet core path (Fig. 11b) vary between 81 and 104 m. Depth variations decrease with increasing latitude. The behavior of the upwelling jet as it oscillates around its initial isobath over the bank is consistent with relative vorticity changes and depth changes partially countering each other to minimize barotropic potential vorticity changes. Furthermore, the depth variations decrease as the across-isobath gradients in potential vorticity increase (with higher f values). The core of the downwelling jet shoals over the bank (Fig. 11c). The jet core moves from the 150-m isobath over the straight shelf to between the 102- and 112-m isobaths at the bank center (Fig. 11d). The downwelling jet shoals the most for the low-latitude run. All downwelling runs exhibit much more isobath departure than the upwelling runs. The downwelling jet bends away from the original isobath over the upstream bank half; this behavior is consistent with the potential vorticity arguments just described.

The potential vorticity is positive everywhere in the upwelling case and negative everywhere in the downwelling case, since the relative vorticity is nowhere large enough (Fig. 7) to change the absolute vorticity sign. The total derivatives in (3a) along the jet path are shown for the upwelling (Fig. 12a) and downwelling (Fig. 12b) cases for the standard midlatitude run. In the upwelling case (Fig. 12a), positive derivatives indicate increasing PV due to either shoaling or relative vorticity increasing (becoming less anticyclonic or more cyclonic). In the downwelling case (Fig. 12b), positive derivatives indicate increasing PV (smaller negative values for $f < 0$) due to either deeper depths or relative vorticity increasing (becoming less cyclonic or more anticyclonic). Barotropic potential vorticity is not conserved in either the upwelling or downwelling case; the total derivative of PV is the same scale as the two component terms. Frictional torque is one reason potential vorticity is not conserved over the bank. The alongstream momentum balance (section 6) indicates the importance of bottom friction, and other studies (e.g., Kurapov et al. 2005) have shown the importance of frictional torques over banks. Even though potential vorticity is not conserved, there is a tendency for relative vorticity changes and

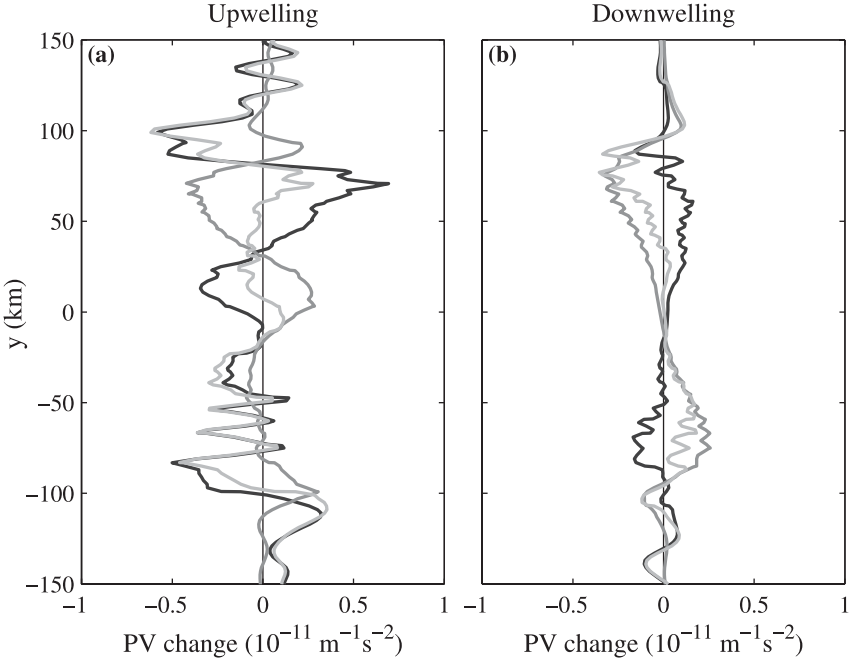

FIG. 12. Changes in barotropic potential vorticity [PV = $(f + \zeta)/h$] along the streamline following the jet core in the standard (a) upwelling and (b) downwelling cases. The thick light gray, dark gray, and black lines indicate $D(\mathrm{PV})/Dt$, $-(\mathrm{PV}/h)Dh/Dt$, and $(1/h)D\zeta/Dt$, respectively.

depth changes to partially counter each other in both cases; the two terms on the right side of (3a) partially offset each other over much of the bank. Because of this tendency, the upwelling jet curves toward its initial isobath, while the downwelling jet tends to bend away. These dynamics lead to pronounced differences in the jet path over the bank: the upwelling jet oscillates about its initial isobath and curves offshore, while the downwelling jet departs from its initial isobath and shoals onshore over the bank.

b. Varying bank dimensions

This section describes upwelling and downwelling circulation in the vicinity of banks with different geometries. Model settings and wind forcing are the same as used in the standard run; only the bank length and width (as defined in section 2) are changed. One set of runs varies length (from 20 to 400 km) while holding width constant at 50 km (the standard run value). The other set varies bank width (from 5 to 70 km) while holding length constant at 200 km (the standard run value). Figures 13 and 14 compare streamline paths for each run in the upwelling and downwelling cases, respectively. In these figures, the streamline that follows the 200-m isobath far upstream of the bank is tracked. The 200-m isobath of each run also is plotted for reference. The first panel in each figure includes the length-varying set of runs, the second panel shows the width-varying set, and the third panel scales all results by length and width. The maximum offshore excursion of this streamline for each run versus bank width is shown in Fig. 15. Offshore excursions for 2D results are included as a benchmark; these excursions are computed by comparing the 2D solutions over the bank and straight shelf.

The streamlines in most upwelling runs follow a similar path relative to the isobaths. All but three runs in the length-varying set (Fig. 13a) have the same across-shelf excursion. The shorter banks (L = 20, 50, 100 km) are the exceptions. The streamlines in these cases move farther offshore and overshoot the bank downstream. The minimum radii of curvature for the 100-, 50-, and 20-km banks are 10, 2.5, and 0.4 km, respectively. The scale for the inertial radius V/f of the flow is 10 km (the inertial radius is 8 km for 80 cm s^{-1} and is 4 km for 40 cm s^{-1}). Thus, the isobath curvature radius r_b of the shortest three banks is near or smaller than the inertial radius ($\mathrm{Ro}_b = V/fr_b \geq 1$). Centrifugal acceleration (and the curvature vorticity) would have to grow large to allow the flow to approximately follow isobaths and bend around these tightly turning banks. Instead, there is extreme separation from isobaths and a pronounced overshoot of streamlines past these banks.

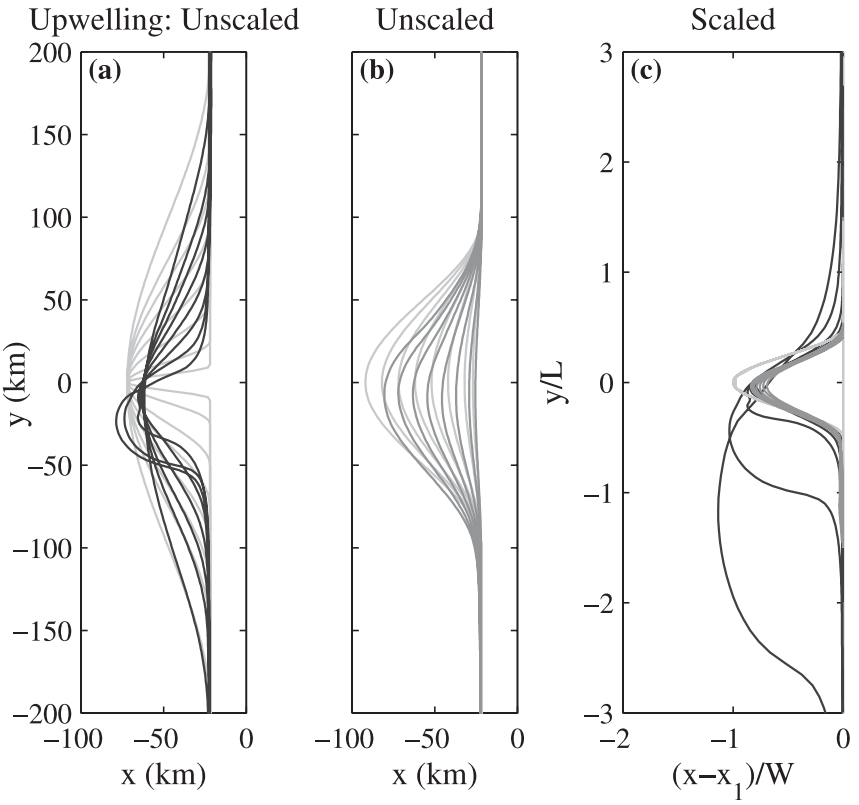

FIG. 13. Streamline path for several upwelling runs (day 10). The selected streamline originates on the 200-m isobath over the straight shelf. The 200-m isobath for each bank also is graphed (thin light gray lines). Two sets of runs were completed: (a) varying bank length while holding width constant at 50 km and (b) varying bank width while holding length constant at 200 km. The results can be (c) scaled by bank length and width; x_1 is the offshore position of the 200-m isobath along the straight shelf.

The upwelling jet passes over much deeper waters as it overshoots these short banks. The streamlines in the runs within the width-varying set (Fig. 13b) detach and reattach to the 200-m isobath at the same location. All banks in the width-varying set have minimum isobath radii of curvature (ranging from 29 to 405 km) that are greater than the inertial radius. The across-shelf excursion of the upwelling jet increases with bank width. Scaling by the bank dimensions (Fig. 13b) collapses the results for all runs except the tightly turning banks where Ro_b is large. For these short banks, the degree of separation increases with bank curvature and the jet path is asymmetric relative to the bank (with a large downstream overshoot). Castelao and Barth (2006) also investigate the conditions leading to separation of an upwelling jet from bank isobaths.

The downwelling runs with varying bank length (Fig. 14a) bend around the bank and have the same offshore excursion, except for the three shortest banks (where $\mathrm{Ro}_b \geq 1$). Similar to the upwelling case, the jet in these short-bank runs overshoots the bank on the downstream side. In contrast to the corresponding upwelling runs, streamlines exhibit less across-shelf excursion than the other downwelling runs. The pronounced departure from tightly turning isobaths in the short-bank runs indicates that the centrifugal acceleration is too small to follow isobaths. Streamlines in the set of runs of varying bank width (Fig. 14b) detach and reattach to the 200-m isobath at the same locations. The across-shelf excursion increases with bank width. Scaling by the bank dimensions (Fig. 14c) collapses results for all runs except those where Ro_b is large. Comparing Fig. 14c to Fig. 13c indicates that offshore excursion (and streamline curvature) is not as large as in the upwelling case. As seen in the standard run, the downwelling jet shoals over the bank and streamlines deviate farther from their initial isobath than in the upwelling case.

The dependence of offshore excursion on bank width is plotted in Fig. 15. The upwelling results all lie on the same line except for the short-bank runs. The downwelling results for runs (excepting the short-bank runs) also exhibit a linear dependence on bank width. The

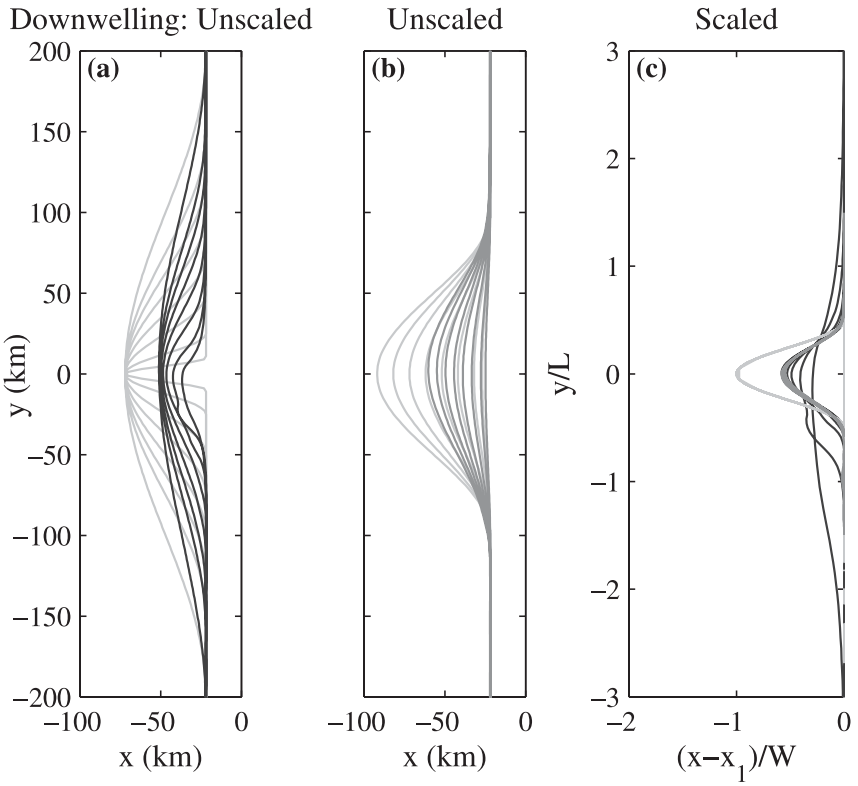

FIG. 14. Streamline path for several downwelling runs (day 10). The panels are described in the Fig. 13 caption.

downwelling trend line is not as steep as the upwelling curve because streamlines are not deflected as far offshore. Streamlines are inshore of their original isobath in most upwelling runs (excepting the short-bank runs) and all downwelling runs. The 3D results are detached more from the coast than the 2D results in both upwelling and downwelling cases. There also is a pronounced asymmetry between 3D upwelling and downwelling results that is not predicted by the 2D results.

The $L = 50$ km, $W = 50$ km run (Fig. 16) is one of the short-bank runs with tightly turning isobaths ($\mathrm{Ro}_b > 1$) with pronounced flow separation in the upwelling and downwelling regimes. As discussed previously, the streamlines and depth-averaged velocity field (Fig. 16) show how the jet overshoots and passes over deeper waters as it flows past the bank. The tendency for the two terms involved in barotropic potential vorticity change (3a) to partially counter each other has different consequences for the two regimes: the upwelling jet tends to curve back toward isobaths, while the downwelling jet tends to curve away from them in response to depth changes. Consequently, the upwelling jet bends farther offshore over the upstream bank half and the downwelling jet remains close to the coast. Neither jet can turn as tightly as the isobaths of this bank without

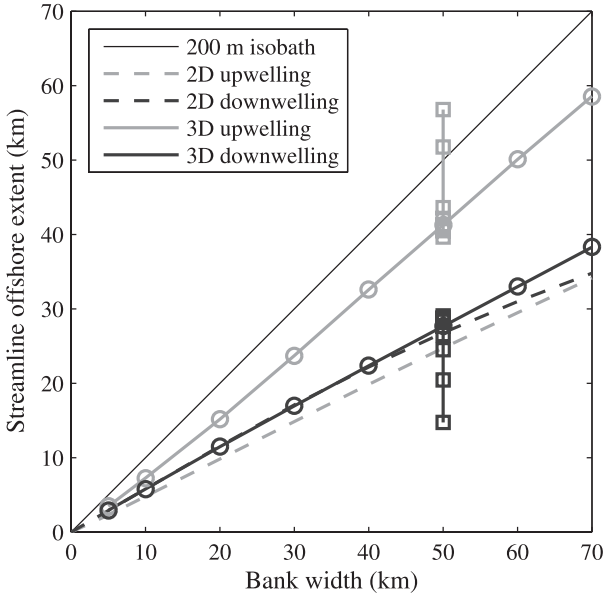

FIG. 15. Across-shelf streamline excursion vs bank width (day 10). This graph measures the maximum offshore excursion (from x_1, the 200-m isobath position along the straight shelf) of the streamline graphed in Figs. 11 and 12. Circles indicate the runs with varying bank width and squares indicate the runs with varying bank length. The three squares with the largest excursion for upwelling and smallest excursion for downwelling are the runs with tightly turning isobaths ($\mathrm{Ro}_b \geq 1$).

extreme centrifugal acceleration. In the upwelling case, the jet flows into much deeper waters over the downstream bank half and farther downstream; it eventually reattaches to its original isobath. In the downwelling case, the jet shoals first then flows over somewhat deeper waters but never moves far offshore. The curvature vorticity values for both cases (not shown) are stronger than over the standard bank but are not strong enough to follow the sharply turning isobaths. The maximum curvature vorticity values ($\pm 0.2f$ for upwelling and $\pm 0.15f$ for downwelling) indicate that the advection term in the depth-averaged across-stream momentum balance flow remains smaller than the geostrophic terms instead of developing enough centrifugal acceleration to approximately follow isobaths around the tightly turning bank. There are similarities between the results from this run and the standard run (Fig. 7) despite the strong flow separation. For the upwelling case, both runs have a strong upwelling jet over the upstream part of the bank with a current reversal inshore of the main jet, and bottom densities increase most at the upstream part of the bank. For the downwelling case, both runs have the smallest bottom density decreases over the bank.

6. Dynamics

This section investigates the dynamics that influence upwelling and downwelling circulation in the vicinity of a bank. Depth-averaged momentum balances for the standard upwelling and downwelling cases are described. Depth-averaged potential density balances and vertical velocities in active areas of upwelling and downwelling also are discussed.

a. Momentum balances

Depth-averaged momentum terms are calculated as part of the ROMS standard diagnostics. Equations (4a) and (4b) are the across-shelf (x) and alongshelf (y) momentum equations In these equations, the overbar denotes depth averaging, η is surface elevation, h is the time-varying depth ($h = \eta + h_o$), ρ_o is the reference density, ρ are the potential densities, τ^{Sx} and τ^{Sy} are the surface stress components, and τ^{Bx} and τ^{By} are the bottom stress components. The dispersion terms in (5) are $G_s = G_x\cos\theta + G_y\sin\theta$ and $G_n = -G_x\sin\theta + G_y\cos\theta$. The dispersion terms are $G_x = (\overline{u'u'}\overline{h})_x + (\overline{u'v'}\overline{h})_y$ and $G_y = (\overline{u'v'}\overline{h})_x + (\overline{v'v'}\overline{h})_y$, where u' and v' are the depth-varying parts of the velocity components. Natural coordinates can be defined by the orientation of transport streamlines (as in section 3): s is positive in the direction of flow, n is positive to the left of the flow, V is the depth-averaged speed, and θ is the flow angle measured counterclockwise from the x axis. These coordinates are used to transform (4) into alongstream and across-stream momentum equations:

$$\frac{1}{h}\frac{\partial \overline{u}\overline{h}}{\partial t} - f\overline{v} = -\frac{1}{h}\frac{\partial(\overline{u}\,\overline{u}\overline{h})}{\partial x} - \frac{1}{h}\frac{\partial(\overline{u}\,\overline{v}\overline{h})}{\partial y} - \frac{G_x}{h} - g\frac{\partial \eta}{\partial x} - \frac{g}{\rho_o h}\int_{-h_o}^{\eta}\left(\frac{\partial}{\partial x}\int_z^{\eta}\rho dz\right)dz + \frac{\tau^{Sx}}{\rho_o h} - \frac{\tau^{Bx}}{\rho_o h} \tag{4a}$$

$$\frac{1}{h}\frac{\partial \overline{v}\overline{h}}{\partial t} + f\overline{u} = -\frac{1}{h}\frac{\partial(\overline{u}\,\overline{v}\overline{h})}{\partial x} - \frac{1}{h}\frac{\partial(\overline{v}\,\overline{v}\overline{h})}{\partial y} - \frac{G_y}{h} - g\frac{\partial \eta}{\partial y} - \frac{g}{\rho_o h}\int_{-h_o}^{\eta}\left(\frac{\partial}{\partial y}\int_z^{\eta}\rho dz\right)dz + \frac{\tau^{Sy}}{\rho_o h} - \frac{\tau^{By}}{\rho_o h}. \tag{4b}$$

$$\frac{1}{h}\frac{\partial Vh}{\partial t} = -\frac{1}{h}\frac{\partial V^2 h}{\partial s} - V^2\frac{\partial \theta}{\partial n} - \frac{G_s}{h} - g\frac{\partial \eta}{\partial s} - \frac{g}{\rho_o h}\int_{-h_o}^{\eta}\left(\frac{\partial}{\partial s}\int_z^{\eta}\rho dz\right)dz + \frac{\tau^{Ss}}{\rho_o h} - \frac{\tau^{Bs}}{\rho_o h} \quad \text{and} \tag{5a}$$

$$V\frac{\partial \theta}{\partial t} + fV = -V^2\frac{\partial \theta}{\partial s} - \frac{G_n}{h} - g\frac{\partial \eta}{\partial n} - \frac{g}{\rho_o h}\int_{-h_o}^{\eta}\left(\frac{\partial}{\partial n}\int_z^{\eta}\rho dz\right)dz + \frac{\tau^{Sn}}{\rho_o h} - \frac{\tau^{Bn}}{\rho_o h}. \tag{5b}$$

The lowest-order depth-averaged across-stream momentum balance is geostrophic. Coriolis acceleration does not enter the alongstream momentum balance (5a); any alongstream pressure gradient is ageostrophic. The following discussion investigates the depth-averaged alongstream momentum balance; all terms are significant over the bank.

The alongstream momentum balance for the upwelling case is shown in Fig. 17; as in (5a), positive values of each term indicate a tendency to accelerate the flow. Local acceleration is strong within the main jet over the bank. The largest values occur on the upstream half of the bank, where jet velocities are highest. The jet is decelerating along the inshore edge and

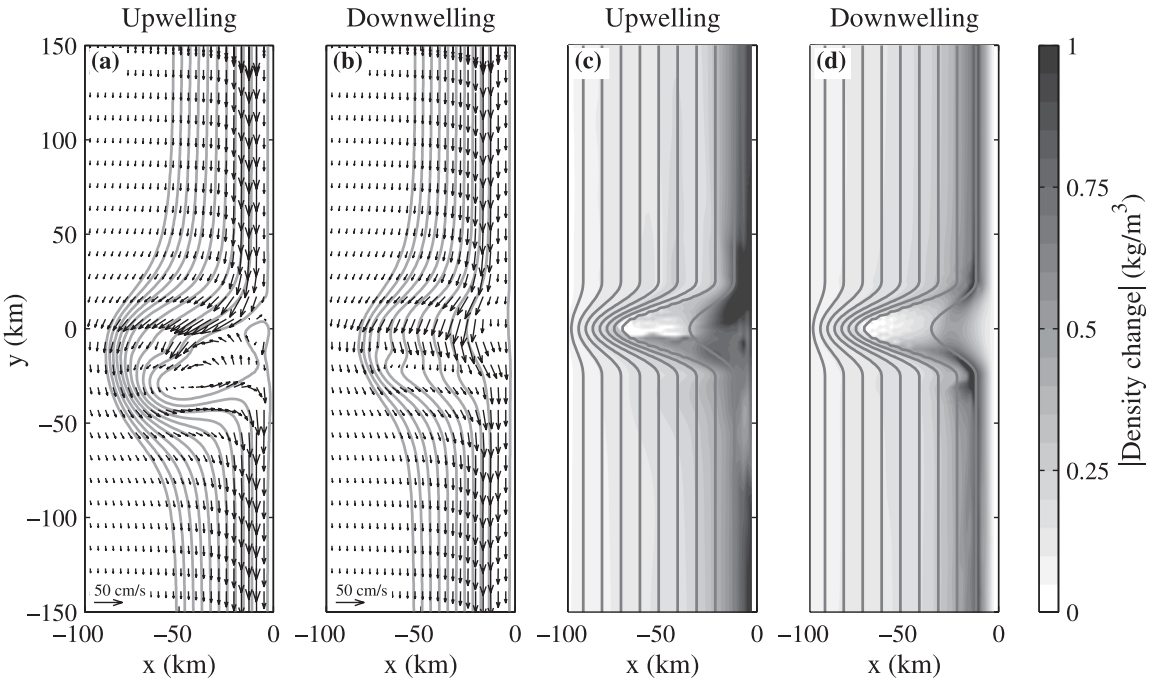

FIG. 16. Depth-averaged velocity vectors and transport streamlines (day 10) during (a) upwelling and (b) downwelling for a bank ($L = 50$ km, $W = 50$ km) exhibiting pronounced flow separation. Bottom density change (day 10) with isobaths contoured at a 100-m interval (gray lines) during (c) upwelling and (d) downwelling. Density increases in the upwelling case and decreases in the downwelling case.

accelerating along the offshore side. This pattern is associated with the continued offshore movement of the jet position. Advection is strongly positive within the jet over the upstream bank half and negative at the downstream bank edge. Momentum is advected over the bank by the upwelling jet, extending the high-velocity region farther over the bank with time. At the downstream bank edge, jet velocities decrease as they are advected into the convergence zone. This deceleration tendency is offset by a favorable alongstream pressure gradient. The ageostrophic pressure gradient is in the opposite direction (negative) over the rest of the bank; it opposes southward flow. This pressure gradient is strongest at the bank center, where it opposes advection. Where the flow is reversed (northward current), the pressure gradient and flow are in the same direction. The pressure gradient tends to balance wind stress in this region and over the downstream part of the bank. Wind stress is spatially uniform, but the alongstream surface stress term is inversely proportional to depth and changes sign where the flow is reversed. The bottom stress decelerates flow close to the coast (where it balances wind stress) and under the advected jet. It is strongest along the inshore side of the jet (over shallower depths). The importance of bottom stress over Heceta Bank has been noted in the modeling studies of Oke et al. (2002) and Gan and Allen (2005).

The momentum balance for the downwelling case is shown in Fig. 18. As in the upwelling case, there is local deceleration along the shoreward side of the jet and acceleration along the seaward side associated with the offshore movement of the downwelling jet. The local acceleration values are smaller than for upwelling because jet velocities are lower and the offshore movement is not as rapid. The downwelling jet remains closer to the coast over the bank than the upwelling jet. Momentum is advected over the upstream bank half by the downwelling jet. The jet velocities decrease as they enter the convergence at the downstream bank edge. The alongstream pressure gradient is important over the bank; it is strongest along the coast. The pressure gradient opposes flow over the upstream part of the bank and tends to accelerate flow at the downstream convergence area (opposing advection and bottom stress). Surface stress is balanced by the pressure gradient (over the upstream half of the bank) and bottom stress. Bottom stress is largest at the downstream edge and is important beneath the advected downwelling jet. As in upwelling, bottom stress is stronger along the inshore side of the jet core position.

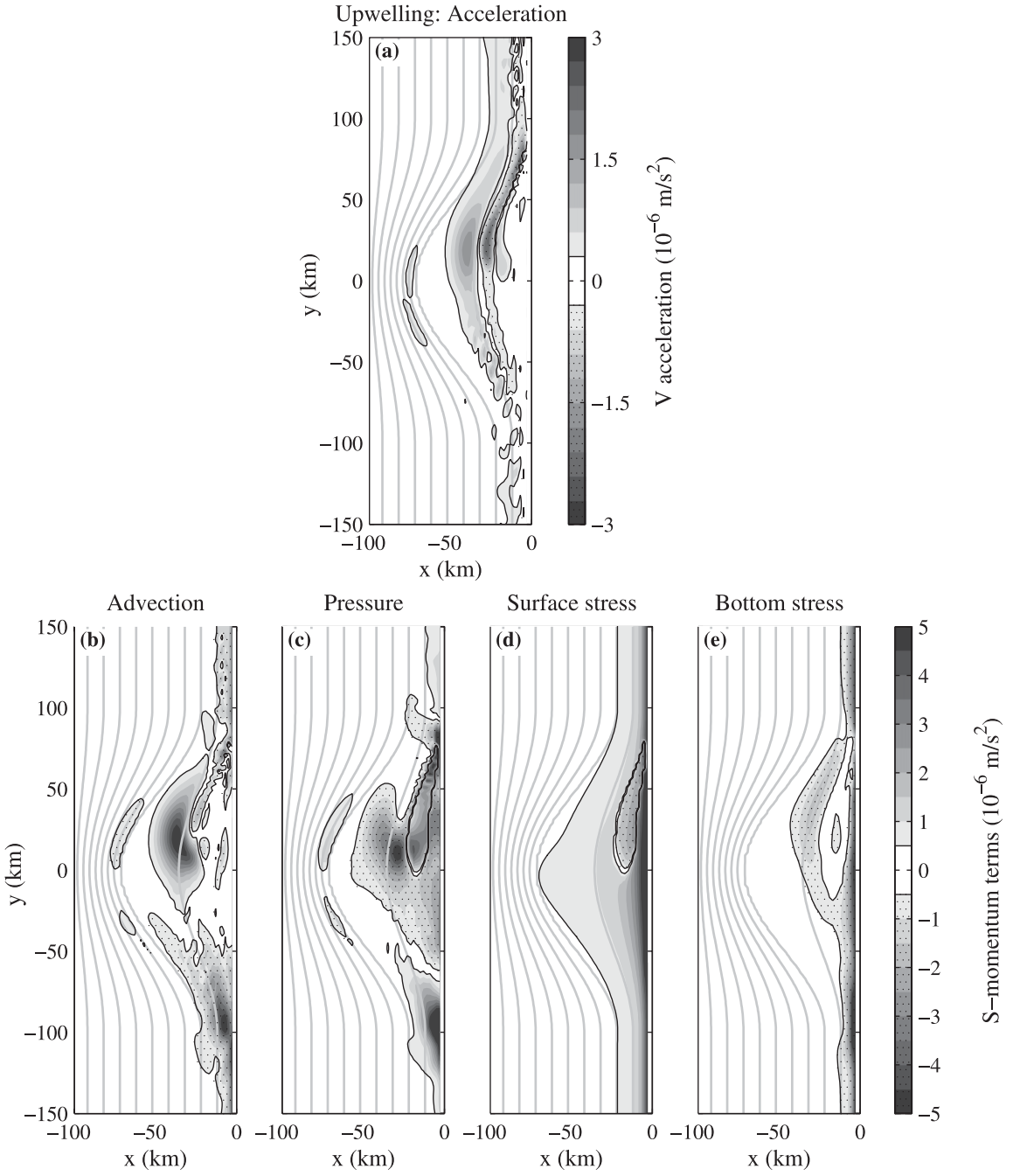

FIG. 17. Depth-averaged alongstream momentum terms for the standard run during upwelling (day 10). The local acceleration is on the left-hand side of Eq. (5a) and all other terms are on the right-hand side. Positive values indicate a tendency to accelerate flow. Isobaths are shown as in Fig. 5.

b. Potential density balance

The depth-averaged density equation helps explain the patterns of density change described in section 4. Density equation terms are calculated as part of the ROMS (version 2.1) diagnostics (ρ is the potential density):

$$\frac{1}{h}\frac{\partial \overline{\rho} h}{\partial t} = -\frac{1}{h}\frac{\overline{\partial u \rho h}}{\partial x} - \frac{1}{h}\frac{\overline{\partial v \rho h}}{\partial y}. \tag{6}$$

The model runs have no surface heat flux and horizontal diffusion is weak, therefore these terms are omitted from (6). Depth-averaged density is only changed by across-shelf

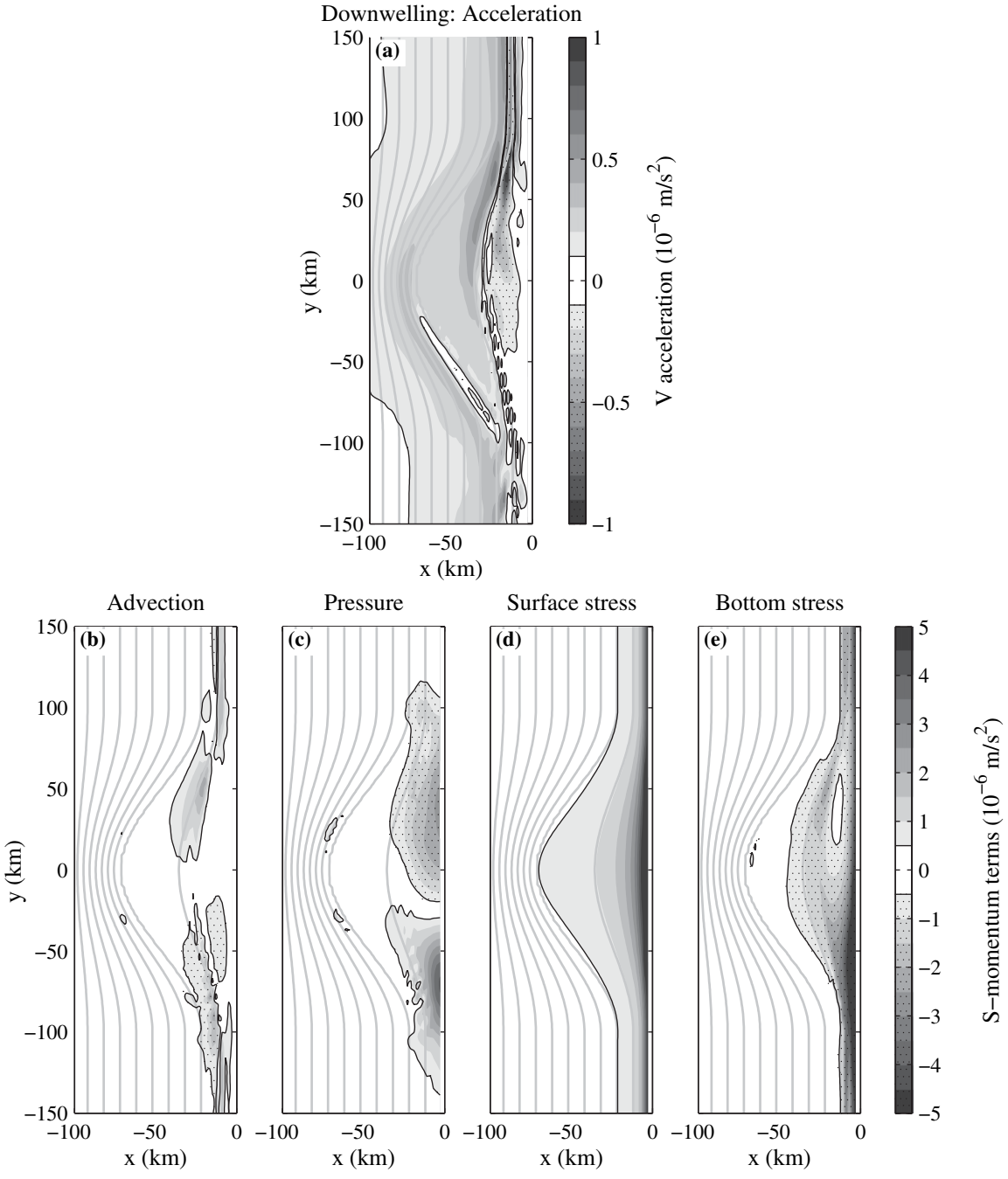

FIG. 18. Depth-averaged alongstream momentum terms for the standard run during downwelling (day 10). The panels are described in the Fig. 17 caption.

(x) and alongshelf (y) advection. As written in (6), the advection terms include contributions from the horizontal divergence terms in the depth-averaged continuity equation. Following Gan and Allen (2005), the horizontal divergence terms and any remaining opposing parts are subtracted from these advection terms for analysis purposes. The resulting net x and y advection terms include only the unbalanced advection that leads to density changes. Subtracting the horizontal divergence terms introduces the continuity term associated with changes in surface elevation: $(\rho/h)(\partial\eta/\partial t)$. This continuity term is subtracted from the density tendency term in (6). Figures 19 and 20 show the density tendency and net advection terms; positive values indicate increasing densities.

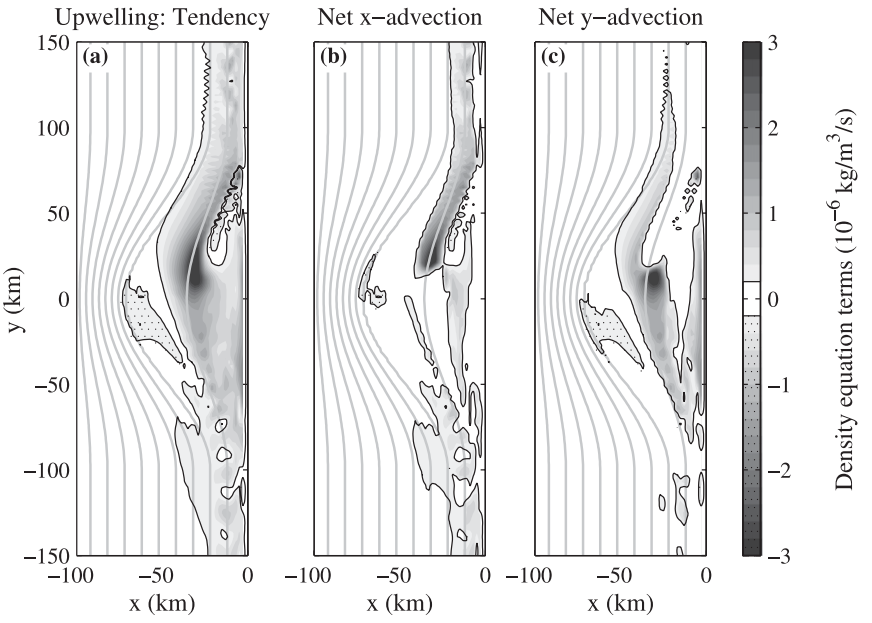

FIG. 19. Depth-averaged density equation terms during upwelling (day 10). The tendency term is on the left-hand side of Eq. (6) and the net advection terms are on the right-hand side. Positive values indicate a tendency to increase density. The net x and y advection terms show only the unbalanced part that effects density change (a large part of the gross advection terms balances partially because of continuity). Isobaths are shown as in Fig. 5.

For the upwelling case (Fig. 19), density increases along the upwelling front. The rate of density change is highest over the upstream bank half. The tendency term also is strong in the jet path over the downstream bank half. Over the straight shelf, across-shelf advection increases densities at the upwelling front (this is consistent with 2D upwelling). Over the bank, both across-shelf and alongshelf density advection are important (indicating 3D effects). Across-shelf advection is associated with upwelling along the front and offshore movement

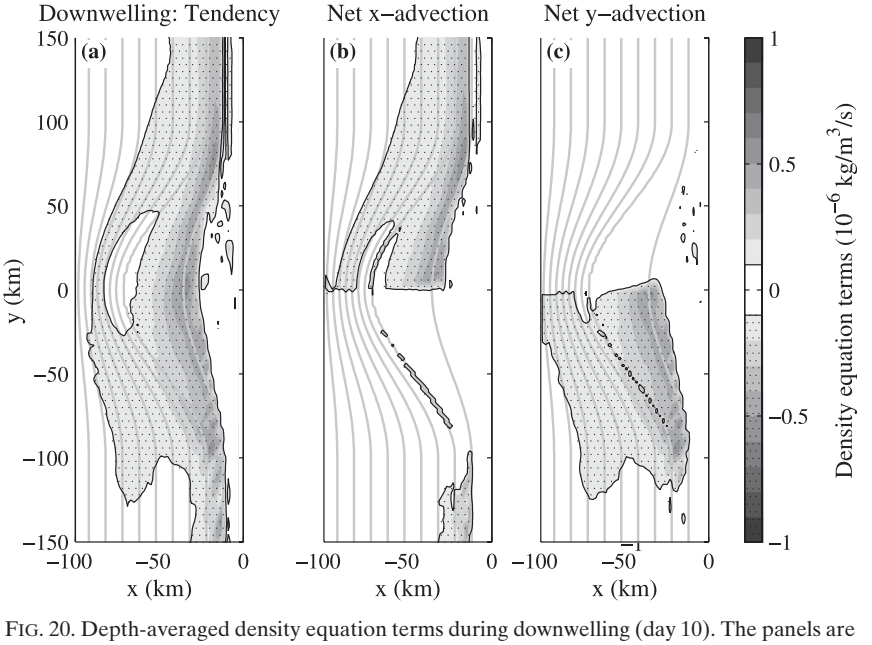

FIG. 20. Depth-averaged density equation terms during downwelling (day 10). The panels are described in the Fig. 19 caption.

of the frontal position. Across-shelf advection dominates along the front over the upstream half of the bank. Alongshelf density advection increases densities along the seaward side of the jet over the upstream bank half, at the leading edge of the dense water tongue (Fig. 5a), and over the downstream bank half. Upwelling creates large density changes at the upstream edge of the bank (Figs. 5a and 6a). The upwelling jet advects this dense water over the bank, forming a dense water tongue. During the first days of winds (not shown), net alongshelf density advection occurs only in this location near the upstream bank edge. After 10 days, the dense water tongue has reached the center of the bank, and alongshelf density advection is extending the dense waters over the downstream half. The density gradient switches sign along the inshore side of the dense water tongue (Fig. 5); this leads to a baroclinic pressure gradient reversal that is associated with a reversal of the depth-averaged pressure gradient and depth-averaged alongshelf flow in this area.

The depth-averaged density balance for the downwelling case is shown in Fig. 20. Density is decreasing along the downwelling front (along the 100-m isobath). The rate of change is smaller than for upwelling and there is less difference between the bank and shelf. Downwelling on the straight shelf occurs through across-shelf density advection. Both across-shelf and alongshelf advection are important on the bank. Across-shelf advection dominates over the upstream half and alongshelf advection dominates over the downstream half. The across-shelf advection associated with the local across-shelf downwelling circulation is augmented by the offshore jet deflection over the upstream bank half and is reduced farther downstream by the bending of the jet back toward the coast. During the first days of winds (not shown), alongshelf advection dominates only near the downstream edge of the bank; this region expands as winds continue. The patterns of across-shelf and alongshelf density advection have some qualitative similarities to the upwelling case. The density changes, however, are of opposite sign; this leads to fundamental differences in the evolution of the density field.

c. Vertical velocity contributions

Regions with large upward or downward vertical velocities indicate active upwelling or downwelling regions. Areas of large density change may not coincide with locations of active upwelling or downwelling because of the importance of alongshelf density advection over the bank. Thus, it is important to identify areas with large vertical velocities and to describe the dynamics creating these upwelling and downwelling zones. Contributions to the vertical velocity at the top of the bottom boundary layer (bbl) are discussed in this section. The approach is similar to Kurapov et al. (2005), except they investigate w at the top of the bottom mixed layer. For the present purposes, the top of the bbl z_1 is defined as the level above the bottom where the magnitude of frictional terms in the depth-varying momentum equations first becomes smaller than 1/10 of the leading term (z_1 varies with location). Where friction is strong throughout the water column (as it is in shallow water near the coast), z_1 is set halfway between the surface and bottom ($z_1 = -h/2$). The vertical velocity at the top of the bbl is expected to include contributions from inviscid flow crossing isobaths producing topographic upwelling and downwelling (w_{topo}) and from bottom stress curl leading to bottom Ekman pumping (w_{pump}); the defining equations (Pedlosky 1987) are

$$w_{\text{topo}}(z_1) = -u(z_1)h_x - v(z_1)h_y \quad \text{and} \tag{7}$$

$$w_{\text{pump}}(z_1) = \frac{1}{\rho_o f}\left(\frac{\partial \tau^{By}}{\partial x} - \frac{\partial \tau^{Bx}}{\partial y}\right). \tag{8}$$

The difference between $w(z_1)$ and w_{topo} is expected to be similar to the w_{pump} field.

In the upwelling case, the vertical velocity at the top of the bbl (Fig. 21a) is upward along the upwelling front over the straight shelf. Over the bank, $w(z_1)$ is upward at the bank center and near the offshore edge along the downstream bank half. The vertical velocity is downward over the upstream bank half between the 100- and 200-m isobaths. The strongest upwelling velocities are in small patches at the upstream edge, center, and downstream edge of the bank. Topographic upwelling (Fig. 21b) contributes to these strong upwelling velocities; the upwelling jet shoals in these areas. There are areas with downward w_{topo} over the upstream bank half, but these only account for part of the active downwelling area in the $w(z_1)$ field. The most prominent features in the w–w_{topo} field (Fig. 21c) are the bands of upwelling and downwelling along the jet path over the upstream bank half. These bands are evidently associated with Ekman pumping due to bottom stress curl (Fig. 21d) along each side of the upwelling jet. Kurapov et al. (2005) point to the importance of Ekman pumping over banks. Ekman pumping contributes to upwelling at the bank center and to downwelling over the upstream bank half.

In the downwelling case, $w(z_1)$ is downward near the coast along the straight shelf (Fig. 22a). There is a narrower band of upward velocities on the offshore side of the downwelling region. These adjacent bands of downwelling and upwelling are evident along the jet path over the bank, though the associated vertical velocities are weaker on the bank. These bands are

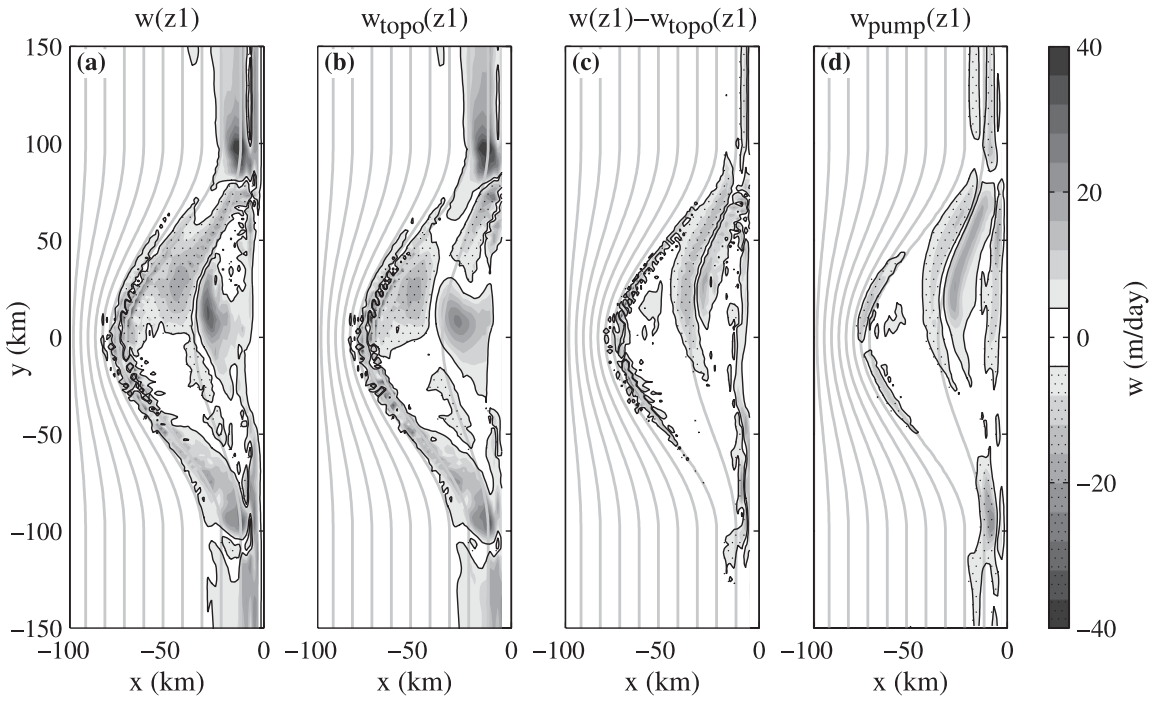

FIG. 21. Vertical velocities at the top of the bottom boundary layer during upwelling (day 10): (a) total vertical velocity, (b) topographic vertical velocity, (c) vertical velocity not due to topographic upwelling or downwelling, and (d) bottom Ekman pumping velocity. Isobaths are shown as in Fig. 5.

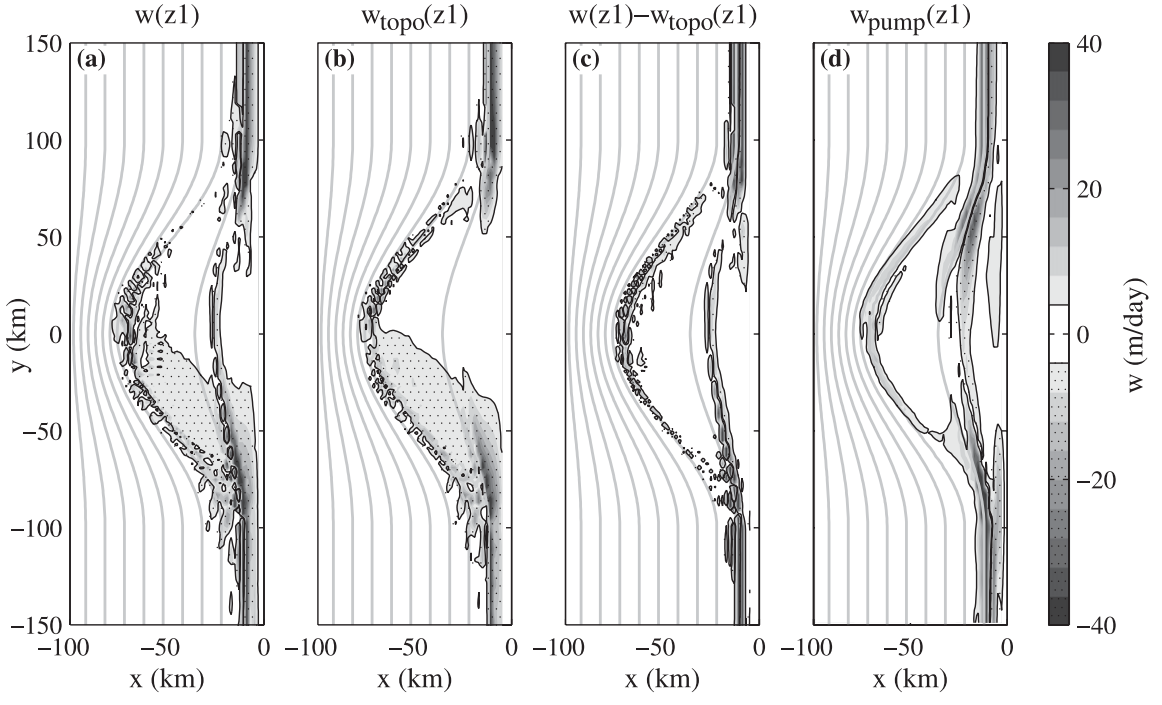

FIG. 22. Vertical velocities at the top of the bottom boundary layer during downwelling (day 10). The panels are described in the Fig. 21 caption.

modulated by ~10-km patterns that likely are associated with baroclinic instabilities in the bottom boundary layer that are the 3D evolution of the symmetric instabilities in the 2D downwelling studies of Allen and Newberger (1996). Vertical velocities are weak over much of the bank. There is a broad area of downward velocities over the downstream bank half and a narrow area of upwelling at the offshore edge over the upstream half; the downwelling and upwelling in these locations are linked to w_{topo} (Fig. 22b). The w–w_{topo} field (Fig. 22c) contains the signature of Ekman pumping (Fig. 22d); the downwelling band is inshore of the upwelling band in this case.

This analysis indicates that topographic upwelling/downwelling and bottom Ekman pumping both make important contributions to vertical velocities over the bank in both the upwelling and downwelling cases. There is striking variation in the $w(z_1)$ fields; only certain areas of the bank show active upwelling or downwelling during upwelling-favorable winds and downwelling-favorable winds.

7. Summary and conclusions

This study investigates how coastal banks along stratified continental shelves influence wind-driven shelf circulation. Banks can generate significant alongshelf variability in the current and density fields and can be areas of asymmetric wind response. Numerical experiments have been conducted to examine upwelling and downwelling dynamics in the vicinity of symmetric banks (with idealized bathymetry). The standard bank (Fig. 1) has similar dimensions to the Heceta Bank complex along the Oregon shelf: its length is 200 km and its width is 50 km. Model runs have a shelf slope and initial stratification representative of conditions along the Oregon coast. The runs are forced with a constant southward wind stress of 0.1 Pa. The sign of planetary vorticity is the only configurational difference between the upwelling ($f > 0$) and downwelling case ($f < 0$). Changing f is equivalent to reversing the wind stress, since the banks are symmetric.

Two-dimensional (without alongshelf variability) upwelling and downwelling have been well studied (e.g., Allen et al. 1995; Allen and Newberger 1996). During upwelling conditions, a baroclinic jet forms (flowing opposite coastal-trapped wave propagation) that is in geostrophic balance with the barotropic and baroclinic pressure gradients; it is in thermal wind balance with upwelled isopycnals. The upwelling front extends throughout the water column and the bottom boundary layer is highly stratified. During downwelling conditions, the geostrophic baroclinic jet flows in the direction of coastal-trapped wave propagation; the near-bottom downwelling front has no surface expression and there is a thick bottom mixed layer. Core velocities in the downwelling jet are slower than in the upwelling jet, partially because there is no near-surface across-shelf density gradient. There are pronounced departures from 2D dynamics over the bank, yet differences in the local 2D dynamics over the straight shelf and the bank center help explain some of the flow characteristics. Compared to the 2D straight-shelf solution, the front in the 2D bank solution is farther offshore (but near the same isobath). Sea level differences between the 2D straight-shelf and 2D bank solutions anticipate alongshelf pressure gradients consistent with the bending of the geostrophic flow around the bank.

The upwelling case for the standard bank indicates flow curves around the bank; the jet core approximately follows the 90-m isobath. There are significant differences between these results and the 2D solution: the upwelling jet and front are much farther offshore over the bank in the 3D solution and there is a current reversal inshore of the main jet. The main upwelling jet is fastest over the upstream bank half. The jet advects a tongue of dense water onto the bank; this switches the sign of the across-shelf density gradient inshore of the main jet. The across-shelf baroclinic pressure gradient reversal leads to the changed sign of the depth-averaged pressure gradient that drives the reversed flow inshore of the main jet. The largest bottom density change is near the coast on the upstream bank half; there is less density change over much of the downstream bank half than on the straight shelf. These results indicate there are regions of intensified upwelling on the bank, but other bank sections have reduced upwelling and even downwelling.

Flow also bends around the bank in the downwelling case, but there is less offshore excursion and less curvature than the upwelling case and there are no current reversals. The downwelling jet core shoals from the 150-m isobath to the 105-m isobath over the bank; the jet moves back to deeper waters over the downstream bank half and returns to its original isobath downstream. The downwelling jet is slowest and widest over the bank. These results are similar to the 2D results, but the jet is more detached from the coast. The flow field is highly symmetric about the bank center. Bottom densities decrease most along the downwelling front (near the 100-m isobath). Unlike during upwelling, there is little density change close to the coast. Only limited density change can take place here because the initial bottom density in shallow waters is close to the density of the surface waters being downwelled. The bank is an area of reduced downwelling. Some of the differences between the

upwelling and downwelling response on the bank are related to the differences in the density field evolution.

The robust differences between the upwelling and downwelling jet paths over the bank are preserved in runs with different planetary vorticity magnitudes. Even though barotropic potential vorticity is not conserved over the bank, the two terms in (3a) contributing to potential vorticity change do tend to partially counter each other. Because of this tendency, the upwelling jet responds to depth changes by curving back toward the original isobath, while the downwelling jet tends to bend away from the initial isobath. This difference causes the upwelling jet to follow isobaths more closely than the downwelling jet (which shoals over the bank).

Results from runs with different bank dimensions reveal that the lowest-order depth-averaged across-stream momentum balance remains geostrophic over all the banks examined. The curvature vorticity (current magnitude divided by the radius of curvature of the flow), which measures the importance of advection in the across-stream momentum balance, is an order of magnitude smaller than f over all banks tested. Streamline paths in most runs collapse to one curve when scaled by bank length and width. The exceptions are banks having an isobath radius of curvature smaller than the inertial radius. This threshold value for the isobath radius of curvature is the same as found in studies of inviscid flows separating from curving coasts and isobaths (e.g., Bormans and Garrett 1989; Klinger 1994; Jiang 1995); however, the dynamics (including frictional effects) and the details of flow separation are different in this study. In the runs exhibiting pronounced flow separation, the jet is farther offshore at the bank during upwelling and closer to the coast during downwelling. In both cases, the main jet remains offshore over deep water far downstream of the bank; both jets eventually reattach to their original isobath. The upwelling jet flows over much deeper waters than the downwelling jet.

All terms in the depth-averaged alongstream momentum balance are important over the bank. There is a striking variation in the primary momentum balances over different bank sections. During upwelling, momentum is advected onto the bank by the strong upwelling jet. The alongstream pressure gradient (ageostrophic by definition) is adverse to southward flow over most of the bank but is favorable to southward flow at the downstream edge. In the reversal area, the alongstream pressure gradient supports the northward currents by balancing wind stress. Bottom friction balances wind stress close to the coast. Bottom stress is strong under the main jet. The momentum balance patterns during downwelling are qualitatively similar to the upwelling case (except for the absence of a current reversal). Bottom stress is stronger over the bank in the downwelling case. In both cases, across-shelf and alongshelf density advection change density on the bank.

Only certain areas of the bank have significant vertical velocities; these are regions of active upwelling and downwelling. There is a complex pattern of upwelling and downwelling occurring over the bank. Vertical velocities at the top of the bottom boundary layer are generated by topographic upwelling and downwelling due to cross-isobath flow and Ekman pumping due to bottom stress curl. Overall, there is intensified upwelling over the modeled bank during upwelling-favorable winds and reduced downwelling over the bank during downwelling-favorable winds. There are marked differences in the currents, densities, and dynamics over different sections of the bank. There are even areas of downwelling in the upwelling case and upwelling in the downwelling case. This part of the model study reveals interesting dynamics for upwelling and downwelling over idealized symmetric banks. These results provide the necessary context for interpreting dynamics over the Heceta Bank complex, the focus of Part II of this study (Whitney and Allen 2009).

Acknowledgments. This study is motivated by the observational and modeling efforts undertaken by the Coastal Ocean Advances in Shelf Transport (COAST) project. The research was supported by the National Science Foundation (NSF) as part of the Coastal Ocean Processes (CoOP) program through the COAST project funded by NSF Grant OCE-9907854. Support for manuscript preparation and publishing was provided by University of Connecticut startup funds.

The authors thank two anonymous reviewers for helpful and constructive comments.

REFERENCES

Allen, J. S., and P. A. Newberger, 1996: Downwelling circulation on the Oregon continental shelf. Part I: Response to idealized forcing. *J. Phys. Oceanogr.,* **26,** 2011–2035.

——, ——, and J. Federiuk, 1995: Upwelling circulation on the Oregon continental shelf. Part I: Response to idealized forcing. *J. Phys. Oceanogr.,* **25,** 1843–1866.

Arthur, R. S., 1965: On the calculation of vertical motion in eastern boundary currents from determinations of horizontal motion. *J. Geophys. Res.,* **70,** 2799–2803.

Barth, J. A., S. D. Pierce, and R. L. Smith, 2000: A separating coastal upwelling jet at Cape Blanco, Oregon and its connection to the California Current System. *Deep-Sea Res. II,* **47,** 783–810.

——, ——, and R. M. Castelao, 2005: Time-dependent, wind-driven flow over a shallow midshelf submarine bank. *J. Geophys. Res.,* **110,** C10S05, doi:10.1029/2004JC002761.

Bormans, M., and C. Garrett, 1989: A simple criterion for gyre formation by the surface outflow from a strait, with application to the Alboran Sea. *J. Geophys. Res.,* **94,** 12 637–12 644.

Castelao, R. M., and J. A. Barth, 2006: The relative importance of wind strength and alongshelf bathymetric variations on the separation of a coastal upwelling jet. *J. Phys. Oceanogr.,* **36,** 412–425.

Dale, A. C., and J. A. Barth, 2001: The hydraulics of an evolving upwelling jet flowing around a cape. *J. Phys. Oceanogr.,* **31,** 226–243.

Durski, S. M., and J. S. Allen, 2005: Finite amplitude evolution of instabilities associated with the coastal upwelling front. *J. Phys. Oceanogr.,* **35,** 1606–1628.

Figueroa, D., and C. Moffat, 2000: On the influence of topography in the induction of coastal upwelling along the Chilean coast. *Geophys. Res. Lett.,* **27,** 3905–3908.

Gan, J., and J. S. Allen, 2005: Modeling upwelling circulation off the Oregon coast. *J. Geophys. Res.,* **110,** C10S07, doi:10.1029/2004JC002692.

Haidvogel, D. B., H. G. Arango, K. Hedstrom, A. Beckmann, P. Malanotte-Rizzoli, and A. F. Shchepetkin, 2000: Model evaluation experiments in the North Atlantic Basin: Simulations in nonlinear terrain-following coordinates. *Dyn. Atmos. Oceans,* **32,** 239–281.

Hill, R. B., and J. A. Johnson, 1974: A theory of upwelling over the shelf break. *J. Phys. Oceanogr.,* **4,** 19–26.

Holton, J. R., 1992: *An Introduction to Dynamic Meteorology*. Academic Press, 507 pp.

Jiang, X., 1995: Flow separation by interfacial upwelling in the coastal ocean. M.S. thesis, School of Earth and Ocean Sciences, University of Victoria, 55 pp.

Johnson, D. R., T. Fonseca, and H. Sievers, 1980: Upwelling in the Humboldt coastal current near Valparaiso, Chile. *J. Mar. Res.,* **38,** 1–16.

Kelly, K. A., 1985: The influence of winds and topography on the sea surface temperature patterns over the northern California slope. *J. Geophys. Res.,* **90,** 11 783–11 798.

Klinger, B. A., 1994: Inviscid current separation from rounded capes. *J. Phys. Oceanogr.,* **24,** 1805–1811.

Kosro, P. M., 2005: On the spatial structure of coastal circulation off Newport, Oregon, during spring and summer 2001 in a region of varying shelf width. *J. Geophys. Res.,* **110,** C10S06, doi:10.1029/2004JC002769.

Kurapov, A. L., J. S. Allen, G. D. Egbert, and R. N. Miller, 2005: Modeling bottom mixed layer variability on the mid-Oregon shelf during summer upwelling. *J. Phys. Oceanogr.,* **35,** 1629–1649.

Mellor, G. L., and T. Yamada, 1982: Development of a turbulence closure model for geophysical fluid problems. *Rev. Geophys.,* **20,** 851–875.

O'Brien, J. J., and H. E. Hurlburt, 1972: A numerical model of coastal upwelling. *J. Phys. Oceanogr.,* **2,** 14–26.

Oke, P. R., and J. H. Middleton, 2000: Topographically induced upwelling off eastern Australia. *J. Phys. Oceanogr.,* **30,** 512–531.

——, J. S. Allen, R. N. Miller, and G. D. Egbert, 2002: A modeling study of the three-dimensional continental shelf circulation off Oregon. Part II: Dynamical analysis. *J. Phys. Oceanogr.,* **32,** 1383–1403.

Pedlosky, J., 1987: *Geophysical Fluid Dynamics*. Springer-Verlag, 710 pp.

Peffley, M. B., and J. J. O'Brien, 1976: A three-dimensional simulation of coastal upwelling off Oregon. *J. Phys. Oceanogr.,* **6,** 164–180.

Rodrigues, R. R., and J. A. Lorenzzetti, 2001: A numerical study of the effects of bottom topography and coastline geometry on the southeast Brazilian coastal upwelling. *Cont. Shelf Res.,* **21,** 371–394.

Shchepetkin, A. F., and J. C. McWilliams, 1998: Quasi-monotone advection schemes based on explicit locally adaptive dissipation. *Mon. Wea. Rev.,* **126,** 1541–1580.

——, and ——, 2003: A method for computing horizontal pressure-gradient force in an oceanic model with a nonaligned vertical coordinate. *J. Geophys. Res.,* **108,** 3090, doi:10.1029/2001JC001047.

——, and ——, 2005: The regional oceanic modeling system (ROMS): A split-explicit, free-surface, topography-following-coordinate oceanic model. *Ocean Modell.,* **9,** 347–404.

Song, Y. T., and D. B. Haidvogel, 1994: A semi-implicit ocean circulation model using a generalized topography-following coordinate system. *J. Comput. Phys.,* **115,** 228–244.

——, ——, and S. M. Glenn, 2001: Effects of topographic variability on the formation of upwelling centers off New Jersey: A theoretical model. *J. Geophys. Res.,* **106,** 9223–9240.

Trowbridge, J. H., and S. J. Lentz, 1991: Asymmetric behavior of an oceanic boundary layer above a sloping bottom. *J. Phys. Oceanogr.,* **21,** 1171–1185.

Weisberg, R. H., B. D. Black, and Z. Li, 2000: An upwelling case study on Florida's west coast. *J. Geophys. Res.,* **105,** 11 459–11 469.

Whitney, M. M., and J. S. Allen, 2009: Coastal wind-driven circulation in the vicinity of a bank. Part II: Modeling flow over the Heceta Bank Complex on the Oregon Coast. *J. Phys. Oceanogr.,* **39,** 1298–1316.

Zaytsev, O., R. Cervantes-Duarte, O. Montante, and A. Gallegos-Garcia, 2003: Coastal upwelling activity on the Pacific shelf of the Baja California Peninsula. *J. Oceanogr.,* **59,** 489–502.